Ultra-fast Kelvin wave packets in Mars' Atmosphere and their Interactions with Tides as Viewed by MAVEN/NGIMS and MRO/MCS

Federico Gasperini [1*], J. Hughes[1], J. M. Forbes[2], and E. M. B. Thiemann[3]

[1]Orion Space Solutions, Louisville, CO, USA
[2]Ann and H.J. Smead Department of Aerospace Engineering Sciences, University of Colorado, Boulder, CO, USA
[3]Laboratory for Atmospheric and Space Physics, University of Colorado, Boulder, CO, USA

Key Points:

- Ultra-fast Kelvin wave (UFKW) packets with 2.5- to 4-day periods and s=-1 are a common and prominent feature of Mars' thermosphere
- UFKW-tide nonlinear interactions produce secondary waves that add strong altitude-longitudinal variability to Mars' thermospheric densities
- Primary and secondary waves are likely to originate below 80 km and propagate to the thermosphere as independent waves

*282 Century Place, Suite 1000, Louisville, CO, 80027

Corresponding author: Federico Gasperini, federico.gasperini@orionspace.com

Abstract

A key element of successful aerobraking operations at Mars is accurate thermospheric density predictions. Evidence suggests that much of the longitude variability in Mars' aerobraking region is associated with atmospheric tides, and the day-to-day variability is connected with tidal modulation by longer-period global-scale waves. Specifically, ultra-fast Kelvin waves (UFKWs) and their modulation of the tidal spectrum play a key role in coupling Mars' lower (<∼80 km) and middle (∼80-100 km) atmosphere with the aerobraking region above. In this study, over 5 years of Mars Atmosphere and Volatile Evolution (MAVEN) Neutral Gas and Ion Mass Spectrometer (NGIMS) CO_2 density observations are employed to reveal prominent, frequent, and persistent 2.5- to 4.5-day UFKW packets in the whole Martian middle and upper thermosphere (ca. 150-200 km), and large secondary waves arising from their nonlinear interactions with the tidal spectrum. Detailed analyses focusing on a prominent ∼2.5-day UFKW event in late 2015 demonstrate primary and secondary wave amplitudes growing twofold with altitude from ∼7-14% near 150 km to ∼12-25% near 200 km and their combined effects to account for ∼60-80% of the altitude-longitudinal variability of Mars' thermospheric density. Concurrent temperature measurements from Mars Reconnaissance Orbiter (MRO) Mars Climate Sounder (MCS) reveal consistent wave signatures near 80 km altitude suggesting propagation of both primary and secondary waves from the lower atmosphere. This study demonstrates that UFKWs and secondary waves from UFKW-tide interactions are sources of significant altitude-longitude variability in the Mars' aerobraking region that should be accounted for when analyzing satellite observations and nonlinear models.

Plain Language Summary

Atmospheric waves with different temporal and spatial scales play a critical role in coupling the lower and upper atmospheres of Mars and cause large perturbations. These waves include solar tides and ultra-fast Kelvin waves (UFKWs). These waves can interact in a nonlinear way to produce secondary waves that propagate away as independent waves. These secondary waves are important because they can add significant variability in longitude and time to Mars' aerobraking region. Here, we analyze over 5 years of thermospheric densities from MAVEN/NGIMS and over 2 years of temperatures from MRO/MCS to show the critical importance that UFKWs and their nonlinear interactions play in Mars' thermosphere. We demonstrate that the tides, the UFKW, and the secondary waves from their interactions (a) are responsible for up to 50-80% of the longitudinal variability in the aerobraking region, (b) grow twofold in amplitude from 150 km to 200 km, and (c) are likely to propagate from the lower atmosphere. These results demonstrate that, similarly to Earth, 2.5- to 4.5-day UFKW packets and secondary waves from their nonlinear interactions produce significant longitudinal variability in Mars' thermosphere and need to be accounted for to anticipate effects due to wave forcing during future Mars' aerobraking operations.

1 Introduction

Atmospheric waves with different spatiotemporal scales are ubiquitous features of all planetary atmospheres. On Mars, their sources are even stronger than on Earth due to the intensive wave-generation processes related to topography, convection, wind shear instability, and frontogenesis in a relatively rarefied atmosphere (e.g., Creasey et al., 2006; Forbes et al., 2020a) and they constitute a significant challenge to our understanding of the state and evolution of the Martian atmosphere and climate (e.g., Yiğit, 2023). Mars' thermosphere (ca. 100-200 km) is strongly coupled with the lower atmosphere below via gravity waves (GWs), planetary waves (PWs), solar tides, ultra-fast Kelvin waves (UFKWs), and with the exosphere above via solar radiation and solar wind particles (e.g., Bougher 1995; Bougher et al., 1999, 2000, 2009, 2015, 2017; Forbes et al., 2008, 2020a, 2023a; Hughes

et al., 2022; Gasperini et al., 2023). It is now well established that atmospheric waves propagating from the lower and middle (below ∼100 km) atmospheric regions are a leading source of longitudinal and day-to-day variability of Mars' thermosphere (e.g., Yiğit, 2023; England et al., 2016, 2017, 2019; Kumar et al., 2022). Of particular interest here are global-scale waves (i.e., tides, PWs, UFKWs) which play a key role in coupling Mars' lower and upper atmospheric regions as they transport momentum, energy, and atmospheric constituents and can interact nonlinearly within each other to produce large thermospheric perturbations important for aerobraking operations (Moudden and Forbes 2010, 2011a,b, 2015; Gasperini et al., 2018). Evidence for global-scale wave coupling into the Martian thermosphere has been presented using accelerometers that measure atmospheric density in the ∼100-150 km region (Tolson et al., 1999; 2005; 2008; Zurek et al., 2017; Gasperini et al., 2018; Jenkins et al., 2023); remotely-sensed observations (England et al., 2016, 2019; Lo et al., 2015; Liu G. et al., 2015, 2017, 2018; Liu J. et al., 2019; Mridula and Manju, 2021; Forbes et al., 2020a, 2023a; Thaller et al., 2020, 2023); and numerical models (e.g., Angelats i Coll et al., 2004; Forbes et al., 2002; Moudden and Forbes, 2011b; Zurek et al., 2017).

Solar thermal tides are prominent examples of global-scale waves driving large longitudinal and day-to-day temperature, wind, and density changes throughout Mars' atmosphere. They are excited by radiative absorption and transfer of CO_2 and by dust and water ice clouds, processes that are significantly influenced by topography, thermal properties of the surface, and dynamics redistributing the absorbing species. Solar tides are generally represented in the form $A_{n,s} = cos(n\Omega t + s\lambda - \Phi_{n,s})$, where λ denotes longitude, Ω is the planetary rotation frequency, s is the zonal wave number, and t is time; and $n = 1$, 2 corresponds to diurnal, and semidiurnal tides, respectively; while s can be positive or negative and the phase speed $-n\Omega/s > 0$ (< 0) corresponds to eastward (westward) zonal propagation. The special case $s = n$ corresponds to a phase speed of $-\Omega$, which is the westward migration speed of the Sun to a ground-based observer. These Sun-synchronous tides are referred to as 'migrating' tides, whereas those that have $s \neq n$ are called 'nonmigrating' tides. Furthermore, converting the above expression for $A_{n,s}$ to the local time frame (t_{LST}), $A_{n,s} = cos[n\Omega t_{LST} + (s-n)\lambda - \Phi_{n,s}]$, we see that from a quasi-Sun-synchronous perspective ($t_{LST} \sim 0$) a tide with zonal wavenumber s and period $n\Omega$ appears as an |s - n| longitudinal variation. The notation DWs or DEs is commonly used to denote a westward or eastward propagating diurnal tide, respectively, with zonal wave number s. For semidiurnal oscillations, 'S' replaces 'D', e.g., the standing oscillations are denoted as D0 and S0. Previous observational and modeling studies (such as those noted above) suggest D0, DW1, DE1, DE2, DE3, S0, SW2, SE1, SE2, and SE3 to be dominant tidal variations in the Martian thermosphere. The predominance of eastward-propagating nonmigrating components in the thermosphere is due to their longer vertical wavelengths (and thus reduced susceptibility to dissipation) than their westward-propagating counterparts. However, it should be noted that the range of tidal components that have so far been derived from observational data at Mars is limited due to asynoptic sampling from current and past missions.

Surface topography and unstable shear flows excite three other groups of atmospheric waves: GWs, PWs, and Kelvin waves (KWs). GWs are essentially local-scale phenomena but can be responsible for significant dynamic and thermal forcing of the global atmospheric state (Yiğit et al., 2008, 2015, 2021). PWs are either quasi-stationary or traveling zonally and are often related to natural quasi-resonances in the atmosphere, but can sometimes arise through, or be amplified by, instabilities, which are enabled by mean wind shears forced by solar inputs and momentum deposited by GWs. KWs are the first equatorially symmetric eastward-propagating gravity-type modes. The shorter period (∼2-6 days) KWs are known as ultra-fast Kelvin waves (UFKWs), and these are capable of extending well into Mars' thermosphere (Gasperini et al., 2018). At Earth, UFKWs are excited by latent heating associated with deep tropical convection in the troposphere, and along with some tides that are excited by latent heat release, essentially carry the

Figure 1. Schematic of nonlinear interaction between two primary waves with frequencies (σ_1), (σ_2) and zonal wavenumbers (s_1), (s_2) and the secondary waves with frequencies (σ_1+σ_2), (σ_1-σ_2) and zonal wavenumbers (s_1+s_2), (s_1-s_2) therein produced. Secondary waves can propagate away from their sources as independent waves and be affected differently by the background wind field depending on their zonal wavenumber and Doppler-shifted frequency.

imprint of tropical troposphere spatial-temporal variability into the upper atmosphere (e.g., Forbes 2000; Gasperini et al., 2015, 2017, 2020). Stationary and traveling PWs do not effectively penetrate into the lower thermosphere, but they do modulate tides through nonlinear interactions (see discussion below); the former with respect to longitude, and the latter in both longitude and time (Moudden and Forbes, 2010; 2011a,b; Forbes, 2017). Similar to solar tides, UFKWs (or PWs) with frequencies $\delta\Omega$ and zonal wave numbers m are commonly expressed as $A_{\delta,m} = cos(\delta\Omega t + m\lambda - \Phi_{\delta,m})$. If $\delta = 0$ the waves are said to be stationary planetary waves (SPWs) with zonal wavenumber m and are designated SPWm. With an analogy to terrestrial observational (e.g., Coy and Hitchman, 1984; Gu et al., 2014; Liu et al., 2015) and modeling (e.g., Lott et al., 2014; Nystrom et al., 2018) studies showing UFKW events to occur over a range of wave periods between about 2 and 6 days, UFKWs in Mars' thermosphere can be considered as a 'wave packet' instead of a monochromatic wave. As discussed in previous terrestrial investigations (e.g., Forbes et al. 2020b, 2023b), UFKWs emanate from specific longitudinal regions, necessitating a distribution of zonal wavenumbers to encompass these localizations and the transience in the forcing results in a distribution of wave frequencies. The resultant wave packet manifests as a constructive-destructive interference pattern arising from the superposition of a spectrum of waves encompassing various frequencies and zonal wavenumbers (e.g., Forbes et al., 2020b). During their vertical propagation, components characterized by a slower phase speed and shorter vertical wavelength undergo selective attenuation, presumably attributed to heightened susceptibility to dissipation and mean wind interactions.

Different components of the global-scale wave spectrum can interact with each other nonlinearly to produce secondary waves that propagate away from their sources as independent waves (e.g., Moudden and Forbes, 2010, 2011a,b; Gasperini et al., 2018). Each secondary wave is affected differently by the background wind field depending on its zonal wavenumber and Doppler-shifted frequency. At some distance from the source, one of the secondary waves could be significantly larger than the other, either due to the propagation conditions or because the two waves are not excited with equal efficiency. These secondary waves are likely responsible for a significant fraction of the spatial-temporal variability in Mars' thermosphere. The interaction referred to here arises because of the nonlinear advection of momentum and heat in the presence of independently generated vertically propagating waves at or below the altitude of interest. Modulation of a tide by a longer period (e.g., 2.5- to 20-day) wave occurs through a nonlinear quadratic interaction that results in the generation of 'sum' and 'difference' secondary waves (Teitelbaum and Vial, 1991). As shown in Figure 1, the interaction between a UFKW with frequency $\sigma_1 = \delta\Omega$ and zonal wavenumber m, $cos(\delta\Omega t + m\lambda)$, and a tide with frequency $\sigma_2 = n\Omega$ and zonal wavenumber s, $cos(n\Omega t + s\lambda)$ yields sum and difference waves with frequencies $n\Omega \pm \delta\Omega$ and zonal wavenumbers $s \pm m$, respectively (note that n and m are integers). Thus, the produced waves have the sums and differences of the time fre-

quencies and zonal wavenumbers, respectively, as their proper frequencies and zonal wave numbers.

In spite of recent progress in diagnosing global-scale waves in Mars' atmosphere, there are many unresolved questions regarding their variability, the secondary waves generated by their nonlinear interactions, and the impacts of the entire spectrum of these waves on Mars' upper atmosphere. The Mars Atmosphere and Volatile Evolution (MAVEN) mission (Jakosky et al., 2015) has been observing the Martian upper atmosphere since late 2014, while the Mars Reconnaissance Orbiter (MRO) mission (McCleese et al., 2007) has been measuring the Martian lower and middle atmosphere since September 2006. These missions have revealed in unprecedented detail the extremely variable nature of the Martian thermosphere and its strong coupling to the lower atmosphere. In this work, over 5 years of CO_2 density observations from the NGIMS instrument onboard MAVEN and about 2 years of concurrent MCS temperature measurements from MRO are examined to reveal evidence of prominent wave coupling associated with ∼2.5 to 5-day UFKW packets, solar tides, and the secondary waves associated with their nonlinear interactions. These analyses provide a unique view into the altitude-dependencies (∼150-200 km) of both primary and secondary waves enabled by the sampling characteristics of NGIMS, which represents a significant advancement over previous investigations of nonlinear wave-wave interactions in Mars' atmosphere (e.g., Moudden and Forbes, 2010, 2011a; Gasperini et al., 2018) that were limited to measurements collected at or below ∼150 km altitude.

After a brief description of the observational datasets (Section 2), Section 3 provides details on the data processing and spectral analysis techniques, Sections 4 and 5 contain results from the analyses of NGIMS CO_2 density and MCS temperature respectively, while Section 6 provides a brief summary and main conclusions.

2 Observational Datasets

2.1 MAVEN/NGIMS CO_2 Density

The MAVEN spacecraft was launched in November 2013 and entered Mars' orbit on 21 September 2014. In November 2014, MAVEN entered its nominal science orbit with an elliptical orbit around Mars at 75° inclination, with a ∼4.5-hr period and periapsis altitude of ∼130-170 km. MAVEN samples five to six longitudes around the planet each Martian day and its orbit precesses through ∼3.5 diurnal cycles per Mars year, i.e., 24 hours of local solar time (LST) are covered every ∼200 days. The Neutral Gas and Ion Mass Spectrometer (NGIMS) instrument onboard MAVEN is a quadrupole mass spectrometer measuring the composition and isotopes of thermal neutrals and ions (Mahaffy et al., 2014, 2015). NGIMS has both open and closed source modes, which enable it to measure both nonreactive and reactive atmospheric species. For each orbit, the number density of each atmospheric species is continuously measured from about 150-200 km altitude, providing an altitude profile of density. These profiles have been used to study thermospheric compositional structure (Mahaffy et al., 2015), density changes associated with small- and global-scale atmospheric waves (e.g., England et al., 2016, 2017, 2019; Liu et al., 2017; Terada et al., 2017; Yiğit et al., 2015; Liu et al., 2017, 2018; Fang et al., 2021).

An overview of NGIMS CO_2 abundance at ∼180 km and its longitude, local time, latitude, and solar zenith angle (SZA) during 2014 - 2020 is provided in Figure 2. The data gaps shown in Figure 2 are largely due to extended deep dip campaigns. Absolute errors are estimated to be less <20% and are considerably lower for mixing ratios (Mahaffy et al., 2015). As detailed in Section 3, the wave diagnostics of NGIMS CO_2 density is performed in terms of percent residuals from the zonal mean. As such, any biases in the density data are minimized when cast in percent residuals from the zonal mean. Previous studies (e.g., England et al., 2016; 2017, 2019; Liu et al., 2017; Forbes et al.,

Figure 2. (a) MAVEN/NGIMS CO_2 Inbound Verified (IV) Level 2 (L2) abundance near 180 km altitude during 2015-2020. (b) Longitude (blue dots, left axis) and latitude (red dots, right axis) of NGIMS measurements in panel (a). (c) Solar zenith angle (blue dots, left axis) and solar local time (red dots, right axis) of NGIMS measurements in panel (a).

2023a) demonstrated NGIMS densities to be well-suited to characterize the global-scale longitudinal variability of interest which ranges between about 5% and 50%.

2.2 MRO/MCS Temperature

MCS is a limb-scanning infrared radiometer launched in 2005 aboard the MRO spacecraft that became fully operational at the end of September 2006 (McCleese et al., 2007). MCS is designed to gather measurements of the Martian surface and atmosphere using various observing geometries, including limb, nadir, and off-nadir measurements. MRO's orbit is nearly polar and Sun-synchronous with an inclination of ∼92.7°. At any given time, MRO is near 3 LST or 15 LST during the ascending or descending parts of the orbit, respectively, except poleward of 75° latitude where the spacecraft shifts from about 15 LST to 3 LST and vice versa in the opposite polar region. The orbital period is ∼112 minutes which translates to nearly 13 passages per day, with each orbit shifted by about 27° in longitude from the earlier one. The MCS observations provide excellent spatial resolution of atmospheric temperatures over the entire planet, from the surface to about 80 km with a vertical resolution of about 5 km and horizontal resolution in the range of 150-300 km depending on altitude. Closer to the surface the errors are ∼0.5 to 3 K, increasing steadily to ∼10 K up to ∼80 km (Guzewich et al., 2012). Prior studies demonstrate that these levels of uncertainty are acceptable for revealing global-scale wave signatures of interest in Mars' atmosphere (e.g., Wu et al., 2015; Guzewich et al., 2012; Banfield et al., 2004; Wilson et al., 2002; Gasperini et al., 2018; Forbes et al., 2020a). The retrieved temperature profiles used in this work are the level 2 data products. The temperatures are interpolated onto a regular altitude grid. This study only employs data near 80 km altitude, although follow-on work may explore propagation of the wave signatures from lower altitudes and potential connections to drivers (e.g., topography, nonlinear interactions, dust).

3 Methods

3.1 Data Processing Technique

Characterization of global-scale waves requires the identification of zonal wave numbers (s) and wave periods ($1/(\delta\Omega)$), which necessitates two-dimensional (2-D) data functions of longitude and time. Techniques such as 2-D fast Fourier transform (e.g., Hayashi, 1971) and 2-D least squares fitting (e.g., Wu et al., 1995) can be applied to the data to determine the amplitudes and phases of such global-scale waves (see the terrestrial study by Yamazaki, 2023). It is possible to perform 2-D spectral analysis on short-time segments of data, and then move the analysis window forward in time to evaluate temporal variations in the global-scale waves. In this work, we extend some of the techniques developed to diagnose waves in Earth's middle atmosphere (i.e., 20-120 km) from temperature profiles made by the Sounding of the Atmosphere using Broadband Emission Radiometry (SABER) instrument on the slowly- precessing Thermosphere Ionosphere

Mesosphere Energetics Dynamics (TIMED) satellite and thermospheric (i.e., ∼260 km) neutral densities determined from quasi-Sun-synchronous Gravity Field and Steady-State Ocean Circulation Explorer (GOCE) satellite accelerometer data (Gasperini et al., 2015; 2017, 2020). Some of these techniques were already successfully applied by Gasperini et al. (2018) to the analyses of MRO/MCS temperature and MAVEN accelerometer (ACC) data, consisting of 2-D least squares fitting and pseudo-longitude spectral analyses.

Prior to performing any spectral analyses, NGIMS data are processed as follows. All inbound verified (IV) NGIMS CO_2 data from late 2014 through early 2020 are averaged onto a 5 km altitude grid from 150 to 200 km on an orbit-by-orbit basis. For example, the average density at 160 km is formed from an average of data from 157.5 km to 162.5 km, with each 5 km cell that typically includes 2 to 3 measurements. Occasionally, there are large outliers in the density that are identified using a 5-point moving window. The criteria used for removing outliers is such that if a measurement is larger than twice the median of the two previous and two following measurements, it is ignored. The median value is used here to minimize negative effects from outliers.

3.2 Spectral Diagnostics

This work employs two different methods to diagnose the spectral characteristics of MAVEN/NGIMS data. Both of these analyses employ the Astropy Python package with a power spectral density (PSD) normalization. A 95% false alarm level of each point is computed in the spectra using the bootstrap method, which is accurate in all normalizations but computationally intensive. Spectral periodicities above this level have a 5% chance of being observed in the absence of a real periodic signal (i.e. false alarm). The spectra are computed in 30-day moving windows. If, in a given window, fewer than 20 points are available the spectrum is not computed.

The first method consists of fitting daily NGIMS data with longitudinal wave numbers 1 (WN1) and 2 (WN2) and then analyzing the spectra of the WN1 and WN2 amplitudes for information about their temporal variation. This analysis is performed in 3 steps by (1) finding the mean density for each day; (2) forming the 'relative abundance' (RA) which is defined as RA = $(A - A_m)/A_m \times 100\%$, where A is the abundance, and A_m is the mean abundance for a particular day (days with fewer than four periapsis measurements necessary to accurately fit WN2 due to the Nyquist criteria are discarded); (3) the cosine waves corresponding to WN1 ($RA_1 = a_1\ cos(\lambda - \Phi_1)$) and WN2 ($RA_2 = a_2\ cos(2*(\lambda - \Phi_2))$) are fit to the data. This analysis is performed in 30-day running windows to be able to resolve periodicities up to about 15 days. Windows containing fewer than 20 measurements are discarded. To establish the significance of any peaks, the spectra are re-computed multiple times to establish the power from pure noise and used to compute the 95% confidence level (CL) for significance, i.e., peaks higher than this CL have a 5% chance of occurring due to random noise.

The second method, developed and employed specifically to investigate secondary waves from nonlinear interactions, is based on prior work (Moudden and Forbes, 2010; 2011a,b; Gasperini et al., 2015, 2017, 2018). This methodology consists of ordering data in pseudo-longitudes λ_p, defined as $\lambda_p = \lambda_p + 2\pi c$, where c is the number of times the entire planet has been covered by MAVEN. This arrangement eliminates the fictitious discontinuity at $0/2\pi$ longitude. The mathematical description of tides and UFKWs remains unchanged. The interaction of a tide with a UFKW yields secondary waves with frequencies equal to $n\Omega \pm \delta\Omega$ and zonal wavenumbers equal to $s \pm m$. When sampled at a nearly constant local time, a tide appears as a wave in the form $cos(n\Omega t_{LST} + (s-n)\lambda_p)$, a UFKW in the form $cos(\delta\Omega t_{LST} + (m-\delta)\lambda_p)$, and the secondary waves in the form $cos[n\pm\delta)\Omega t_{LST} + ((s\pm m) - (n\pm\delta))\lambda_p]$. These various zonal wavenumbers for different existing tides, UFKWs, and their secondary waves each contribute to the zonal variability in any atmospheric field. Spectral analysis of a given time series of space-based

Figure 3. Period (2 to 7.5 days) versus zonal wavenumber (s ± 2) spectrum of NGIMS CO_2 abundance near 180 km obtained by performing 2-D least squares fitting on all the data sampled during 2015-2020. A clear periodicity near 2.5 days and s = -1 is found that is evidence of prominent (5-year averaged amplitudes up to ∼3%) ∼2.5-day ultra-fast Kelvin waves with s=-1 (UFKW1s). Other important periodicities shown in the spectrum occur at ∼3.5 days and ∼7 days, both with s = 0.

measurements as described above can reveal the dominant values of $(s - n)$, $(m - \delta)$ and $((s \pm m) - (n \pm \delta))$, and subsequently the dominant tides, UFKWs, and any UFKW-tide modulations. Note that tides appear as integers, and one cannot differentiate between a UFKW and the UFKW modulation of a migrating tide (|s - n| = 0). Although these secondary waves are not retrievable from normal time series analyses, they are identifiable in the pseudo-longitude spectrum due to the specificity of their space-based wavenumbers. The pseudo-longitude spectral analysis is performed by applying a Lomb-Scargle Periodograms (LSP) method (VanderPlas, 2018) to NGIMS data in 30-day moving windows. The method assumes local time to be constant in each window (NGIMS data precess by about 3 hours over 30 days), which is deemed to be an acceptable approximation as discussed in prior work (e.g., Gasperini et al., 2018). It should be noted that there exists a difficulty when analyzing MAVEN/NGIMS data using LSP due to the sampling characteristics with 4-5 periapsis measurements per day separated by ∼66° of longitude. The Nyquist limits the maximum resolvable wave number in the LSP to about 360°/(2 x 66°) ∼2.7 and wave numbers higher than |s - n| ∼2.7 may be aliased about this 'virtual boundary'. For instance, a 'true' wave number periodicity occurring at |s - n| = 3 would appear at |2.7 – (3 - 2.7)| ∼2.4. Thus, to eliminate this aliasing effect, before performing the LSP each 30-day-long pseudo-longitude series is 'folded' into 7 consecutive days/cycles and stepped forward one day/cycle at the time, i.e. FPL = PL % (7 x 360°) where 'FPL' is the folded pseudo-longitude and 'PL' is the true pseudo-longitude. This 'folding' greatly reduces the spacing between each periapsis measurement, and thus largely eliminates the aliasing.

4 MAVEN/NGIMS CO_2 Wave Analyses

A 2-D least squares fitting technique is applied to NGIMS CO_2 relative abundances, as described in Section 3.1, by (a) combining all data collected during 2015-2020 and (b) in 30-day moving windows. Figure 3 contains the period-wavenumber amplitude spectrum of NGIMS CO_2 relative abundances near 180 km altitude for case (a), showing periods between 2 and 7.5 days and zonal wavenumbers $s \pm 2$. This ∼5-year mean spectrum shows a large (∼3.5%) periodicity at ∼2.5 days and s = -1 that is evidence of prominent UFKW1 (i.e., UFKW with s = -1) activity during this period. While not completely unexpected based on prior work by Gasperini et al. (2018), which was limited to an 18-day period in 2016 near the autumnal equinox, the UFKW1 signature evidenced in Figure 3 is particularly striking when considering that all latitudes sampled by NGIMS during this ∼5-year period are included in the analysis. Other prominent wave components present in Figure 3 are zonally symmetric ($s = 0$) and have periods near 3.5 and 7 days. As noted by Gasperini et al. (2018), these $s = 0$ may be due to the dissipation of tides that are modulated at PW periods. In the terrestrial thermosphere, Forbes et al. (2018) provided modeling evidence that a dissipating tidal spectrum modulated by PWs causes

Figure 4. (a) Period (2 to 4.5 days) versus time (2015-2020) structure of UFKW1 amplitudes near 180 km obtained least squares fitting NGIMS CO_2 abundance in 30-day moving windows. (b) Time series of 2.5-day UFKW1 amplitudes highlighting the two periods between 17 November 2015 - 17 December 2015 and 29 May 2018 - 17 June 2018 with particularly large amplitudes (above 20%). (c) Period (2 to 6 days) versus zonal wavenumber ($s \pm 2$) spectrum of NGIMS CO_2 abundance near 180 km during 17 November 2015 - 17 December 2015. (d) Same as panel (c), but for 29 May 2018 - 17 June 2018.

the thermosphere to 'vacillate' over a range of PW periods. Further observational analyses, outside of the purview of the current study, should explore the sources of these zonally-symmetric oscillations in Mars' thermospheric densities, and their plausible connections to PWs and UFKWs.

Next, we derive the UFKW1 amplitude spectrum for periods between 2.5 days and 4.5 days applying least squares fitting to 30-day moving windows (i.e., case (b)). Figure 4a contains the period-time structure of UFKW1 amplitudes near 180 km during 2015-2020, while Figure 4b shows the corresponding time series of 2.5-day UFKW1 amplitudes. Prominent 2.5- to 4-day UFKW1 packets are found to occur in Mars thermospheric density throughout 2015-2020. The 2.5-day UFKW1 is shown to be more prominent and persistent compared to longer-period UFKW1s. This finding is in general agreement with the understanding that shorter-period waves tend to possess longer vertical wavelengths and thus are less susceptible to dissipation. With analogy to previous terrestrial studies (e.g., Forbes 2000; Forbes et al., 2009), it is known that during their vertical propagation from the lower atmosphere, UFKWs characterized by a slower phase speed and shorter vertical wavelength undergo selective attenuation, presumably attributed to heightened susceptibility to dissipation and mean wind interactions. This behavior would explain larger amplitudes and frequency for the 2.5-day UFKW1 compared to longer period UFKW1s. Days with amplitudes above 10% are highlighted with blue open circles in Figure 4b, while the two intervals with enhanced (exceeding ∼20%) 2.5-day UFKW1 amplitudes are marked with vertical lines. These two periods correspond to 17 November - 17 December 2015 and 29 May - 17 June 2018. Note that the mid-2016 period, showing amplitudes up to ∼12%, was the one investigated in detail by Gasperini et al. (2018). A closer examination of Figure 4a reveals a clear correlation between wave amplitudes and latitudes (white open dots). The largest amplitudes generally occur at low latitudes consistent with the equatorially-trapped nature of UFKWs. However, it should be noted that significant variations are also found at mid-latitudes that may be related to mean wind effects (e.g., Bougher et al., 2015). This result suggests the possible occurrence in Mars' thermosphere of UFKWs at middle (and potentially high) latitudes that should be investigated in further detail in dedicated modeling and observational studies. Figures 4c and 4d show the period-wavenumber spectra of CO_2 abundances during the two periods of 'exceptionally' large (above ∼15%) UFKW1 amplitudes, demonstrating the predominance of ∼2.5-day s = -1 variability. Also present during 17 November - 17 December 2015 is a large (∼8%) westward ∼4-day s = 1 PW, while during 29 May - 17 Jun 2018 a ∼5.5-day s = 0 zonally-symmetric oscillation exhibits significant (∼12%) amplitudes.

Similarly to PWs, UFKWs can modulate the tidal spectrum and their signature may generate variability in the longitudinal WNs at the UFKW period. Figure 5 explores

Figure 5. Period (2-6 days) versus time (1 September - 1 December 2015) structure of the longitudinal wavenumber 1 (WN1, panel a) and longitudinal wavenumber 2 (WN2, panel b) obtained fitting 'daily' NGIMS CO_2 abundances near 180 km. The red contour lines indicate a 5% false alarm level (i.e., peaks inside these boundaries have a less than 5% chance of occurring in the absence of a real periodic signal). WN1 and WN2 show large and persistent variations near 2.5-3.5 days, which are later demonstrated to be associated with a prominent UFKW1 packet.

Figure 6. (a) 2-D pseudo-longitude (FPL) versus time amplitude spectrum during 17 November 2015 - 1 December 2015 obtained using 30-day moving windows of NGIMS CO_2 abundance measured near 180 km. The red contours in panel (a) indicate a 5% false alarm level, while the dashed white vertical lines highlight November 21 and November 28. (b) Pseudo-longitude amplitude spectra were computed using 30-day windows centered on November 21 (blue line) and November 28 (orange line). Dominating the spectra are periodicities near |s - n| = 2.4, 1.4, 1.0, and 0.4.

the period-temporal variability of WN1 and WN2 amplitudes during September-November 2015, corresponding to the first (and most significant) UFKW1-enhanced interval shown in Figure 4b. Wave amplitudes are derived on a daily basis using least squares fits on relative abundances of NGIMS CO_2, as detailed in Section 3.1. On a nearly constant LST (such as that of NGIMS observations over ∼30-day periods), WN1 is likely produced by a combination of D0 and SPW1, while WN2 is likely to originate from a superposition of DE1, SPW2, and S0. Note that Forbes et al. (2021) reported SPW2 to be a primary contributor to the WN2 density variations measured by the accelerometer on the ExoMars Trace Gas Orbiter (TGO). SPWs are generally not linked to thermospheric dynamics on Mars, however, since SPWs arise due to the interactions between the largest tidal components in the Martian thermosphere, it is possible for them to have significant amplitudes (Forbes et al., 2021). Clearly dominating the temporal variability of the WN1 and WN2 amplitudes shown in Figures 5a and 5b are large (up to ∼14%) ∼2.5-day to ∼3.5-day variations. These longitudinal WNs are independent of sign (i.e., both eastward and westward propagating), however, based on the spectral results presented in the later part of this article, these variations can be interpreted as further evidence for the interaction between the tidal spectrum and the UFKW1 packet. Also present are modulations near 4.5 days likely associated with PW activity with $s = 1$ (ref. Figure 4c).

As demonstrated by Gasperini et al. (2018) using MAVEN/ACC data (and discussed in Section 1), UFKWs can interact nonlinearly and the secondary waves therein produced can propagate as independent waves. It is thus of compelling scientific value to investigate the presence and impacts of possible UFKW-tide interactions during November 17 - December 17, 2015, a 30-day period with the largest UFKW amplitudes observed by NGIMS. Figure 6a shows the 2-D FPL spectrum of NGIMS CO_2 relative abundances near 180 km altitude, computed using 30-day moving windows, as a function of day-of-

Figure 7. (a) Altitude (150-200 km) versus pseudo-longitude (FPL) wavenumber (|s - n| = 0.1 - 2.7) amplitude spectrum of NGIMS CO_2 abundance computed using a 30-day window centered on 21 November 2015. (b) Altitude progression of the dominant wave components near 0.4 (blue line), 1.0 (orange line), 1.4 (green line), and 2.4 (red line) for a 30-day window centered on 21 November 2015 (solid lines) and 28 November 2015 (dashed lines).

Figure 8. Altitude (150-195 km) versus longitude (-180° to +180°) reconstructions for the pseudo-longitude periodicities |s - n| near 0.4 (a), 1.0 (b), 1.4 (c), 2.4 (d), 3.0 (e), 4.0 (f) in NGIMS CO_2 abundance for the 30-day window centered on 21 November 2015. The 'total' reconstruction that includes the superposition of panels (a)-(f) is shown in (g). The observed altitude-longitude structure of NGIMS CO_2 abundance is shown in (h). Data are shown as variations over the longitude mean calculated at each altitude (in 5 km steps). The total reconstruction is shown to capture most of the longitude variability in the observations at all altitudes. Moreover, the secondary waves near 0.4 and 2.4 are seen to add altitude-longitude variability (up to about ±20%) that is comparable with that of the primary waves producing them.

year (doy) extending from November 17 through December 1, 2015, and up to WN=2.7. Figure 6b shows the corresponding wave spectra centered on November 21 (blue line) and November 28 (red line). Prominent (>10%) periodicities are found to occur near |s - n| = 0.4, 1.0, 1.4, and 2.4. The 1.0 (i.e., WN1) variation is likely to correspond to D0 or SPW1, as discussed for Figure 5a, while the 1.4 variation is consistent with a 2.5-day UFKW1 (|s - n| = |(-1) - (1/2.5)| = |-1 - 0.4| = 1.4). Remarkably, large (∼12-17%) periodicities are found near |s - n| = 0.4 and 2.4 evidence of secondary waves originating from UFKW1-WN1 interactions.

The corresponding 30-day-mean altitude-doy plot, centered on November 21, 2015 and extending from 150 km to 200 km, is shown in Figure 7a. Figure 7b shows the altitude evolution for primary and secondary waves for the periods centered on November 21, 2015 (solid lines) and November 28, 2015 (dashed lines). Figure 7b demonstrates primary and secondary wave amplitudes growing twofold with altitude in the thermosphere from ∼7-12% near 150 km to ∼14-25% near 200 km. These amplitude variations with altitude conform to theoretical expectations for vertically propagating tides in a diffusion-dominated Mars atmospheric regime. Forbes et al. (2002) predicted wave amplitudes to have a monotonic increase with altitude or to be near-constant. Their numerical results, employing a simple linear model of tides in the thermosphere, suggest that density perturbations monotonically increase with altitude by about a factor of ∼2 between 140 km and 200 km. This result is consistent with the growth of the wave amplitudes in Mars' middle and upper thermosphere shown in previous observational studies (e.g., Liu et al., 2017; England et al., 2017, 2019; Fang et al., 2021). The growth of both primary and secondary wave amplitudes with height in the 150-200 km altitude region at Mars is particularly significant as this region is critical for aerobraking maneuvers.

Figure 9. (a) Period (2-4.5 days) versus time (1 January 2015 - 31 January 2017) contour plot of UFKW1 temperature amplitudes near 80 km from MRO/MCS near ±10° latitude. (b)-(c) latitude versus time structure of the corresponding 2.5- and 3.5-day UFKW1s, respectively. Highlighted with white vertical lines and labels is the period between 17 November 2015 and 17 December 2015 displaying prominent UFKW1-tide interactions in MAVEN/NGIMS thermospheric CO_2 abundance (ref. Figures 5-8). The white open circles in panels (b)-(c) indicate the approximate latitude locations concurrently sampled by NGIMS.

Next, we use the specific frequencies diagnosed in Figure 6 to investigate the altitude-longitude variability of primary and secondary waves. These altitude-longitude reconstructions for NIGMS/CO_2 densities centered on 21 November 2015 are conducted in 5 km altitude intervals from 150 km to 200 km for |s - n| = 0.4 (panel a), 1 (panel b), 1.4 (panel c), 2.4 (panel d), 3 (panel e), and 4 (panel f). The values are expressed as % variations on the mean abundance at each altitude interval. The full reconstruction that includes the superposition of all of these WNs is shown in Figure 8g and compared with the original PL-sampled data (Figure 8h). Clear longitudinal variations are apparent in the observed data. The total fit (Figure 8h) reproduces the salient longitudinal features found in the observations (Figure 8g), indicating that the sum of wave-1, wave-3, wave-4, the 2.5-day UFKW1, and the secondary waves due to UFKW-tide interactions can adequately describe most (∼60-80%) of the altitude-longitude variability. A close examination of Figures 8a and 8d and comparison with Figures 8h, one can see the importance of secondary waves in explaining the observed altitude-longitudinal variability (Figure 8h). Figure 8 demonstrates that the contribution of secondary waves to the total longitude variation can be quite large (up to about ±20%). This result, along with those in Figure 5, demonstrates that wave-wave interactions are responsible for important longitudinal-temporal variability and should be accounted for when analyzing thermospheric variability in nonlinear models and satellite data in the Mars' thermosphere.

5 MRO/NGIMS CO_2 Wave Analyses

Section 4 demonstrates that 2 to 4.5-day UFKW1 packets are a common and prominent feature of Mars' thermospheric density. Moreover, nonlinear interactions involving UFKW1 packets are shown to generate secondary waves with amplitudes that can be as large as the waves producing them. In this section, remotely-sensed neutral temperature observations from MRO/MCS near 80 km altitude are examined to determine whether these UFKW packets and the associated secondary waves due to their nonlinear interactions may be propagating from the middle atmosphere.

Figure 9a shows the period-temporal structure of UFKW1 temperature amplitudes near the equator (±10° latitude) and ∼80 km altitude during January 2015 - January 2017 from MRO/MCS temperatures. Strong (∼10 K) 2.5- to 4.5-day UFKW1 packets are found to occur throughout 2015-2016. The ∼2.5-day UFKW1 is shown to be dominant compared to longer-period UFKW1s. This finding is not unexpected as shorter-period waves tend to have longer vertical wavelengths and thus be less susceptible to dissipation (as discussed in Section 1 and in the context of Figure 4a). Of particular interest is the November 17 - December 17, 2015 period when prominent UFKW1, WN1, and secondary waves are observed in NGIMS data sampling the 10°N to 40°N latitude re-

Figure 10. Pseudolongitude power spectrum of MCS temperatures near 80 km altitude obtained from ascending/descending node difference fields during 17 November 2015 - 17 December 2015 and ±30° latitude. All the main periodicities observed in the spectrum are consistent with the primary waves: 3.5- and 2.5-day UFKW1s (|s - n| at ∼1.3 and ∼1.4, respectively), D0 (|s - n| at ∼1.0) and DE1 (|s - n| at ∼2.0), and the secondary waves due to their nonlinear interactions: S^{-}_{1A}, S^{+}_{1A}, S^{-}_{2A}, S^{+}_{2A}, S^{-}_{1B}, S^{+}_{1B}, S^{+}_{2B} (|s - n| near 2.3, 0.3, 3.3., 0.7, 2.4, 0.4, and 0.6, respectively). A legend for these periodicities is provided to the right of the spectrum.

gion (ref. Figures 5-8). During this ∼30-day period, MCS temperatures are found to display a large (∼8 K) and well-defined UFKW1 packet with dominant periodicities near 2.5 and 3.5 days. Figure 9b (Figure 9c) shows the latitude (±60°) - temporal (January 2015 - January 2017) structure of 2.5-day (3.5-day) UFKW1 temperature amplitudes measured by MRO/MCS near 80 km altitude. Overplotted with white open circles are the approximate latitude locations sampled by NGIMS. Note that NGIMS latitude sampling occurs near 20°N-30°N during the maximum 2.5-day UFKW1 observed by MCS, nevertheless, NGIMS is shown to capture significant 2.5-day UFKW1 amplitudes even in these mid-latitude regions (see discussion in Section 4). Both the 2.5- and 3.5-day UFKW1s demonstrate their largest amplitudes at low latitudes but also display significant latitudinal asymmetries. This result is consistent with previous analyses of MCS data (e.g., Gasperini et al. 2018) and, by analogy with previous terrestrial studies (e.g., Forbes 2000, 2020b; Gasperini et al., 2015), may be explained by the effect of mean winds. Further work focusing on connecting mean winds with vertical wave propagation through the thermosphere is warranted.

Finally, we apply a method to infer the 'diurnal' period waves in the observed temperature perturbations leveraging the sun-synchronous orbit of MRO with equatorial crossing times near 3 LST and 15 LST (e.g., Lee et al., 2009; Guzewich et al., 2012, 2014). The method consists of examining the sum and difference temperature fields that are ∼12 hr apart in LST, allowing for the separation of the diurnal components from the semidiurnal components, and thus for the separation of odd and even tidal harmonics. That is, odd harmonic tides (i.e., diurnal, terdiurnal, etc. components) are out of phase during the ascending and descending portions of the orbit, so the difference between observations made at similar latitudes along those tracks contains only odd tidal harmonics. The ascending/descending node difference fields are here referred to as 'ADND', similar to the terrestrial study by Gasperini et al. (2022). Conversely, the sum of observations made at similar latitudes along the ascending and descending tracks contain the longitude mean plus even tidal harmonics (i.e., semidiurnal, quarterdiurnal, etc., components). The ADND is applied to MCS temperatures near 80 km for the whole 2-year period shown in Figure 9 to help identify potential tidal components involved in the nonlinear interactions shown in Figures 5-8.

The pseudo-longitude spectrum of MCS ADND temperatures near 80 km and ±30° latitude during November 17 - December 17, 2015 is contained in Figure 10. The method used to produce the pseudo-longitude spectrum in Figure 10 is detailed in Section 3.2 (and is identical to that adopted by Gasperini et al., 2018). The latitude range extending from ±30° is chosen to capture the large UFKW1 amplitudes observed in MCS data near 80 km during this ∼30-day period (ref. Figures 9b and 9c). Figure 10 shows large periodicities near |s - n| = 1.0, 2.0, 1.3, 1.4 that are evidence of the signatures of D0 (24h, S0) (marked in red); DE1 (24h, E1) (marked in green); 3.5-day UFKW1 (84h, E1) (marked

in brown as 'KW_A'), and 2.5-day UFKW1 (60h, E1) (marked in blue as 'KW_B'), respectively. Note that contributions from semidiurnal tides and SPWs are removed when computing ADND fields. Remarkably the pseudolongitude spectrum in Figure 10 demonstrates several other periodicities that can be explained by nonlinear interactions among the above primary waves. The resulting secondary waves (color-coded and labeled according to the interacting UFKW1) produce prominent periodicities near |s - n| = 2.3 (S^-_{1A}), 0.3 (S^+_{1A}), 2.4 (S^-_{1B}), 0.4 (S^+_{1B}), 3.3 (S^-_{2A}), 0.7 (S^+_{2A}), 0.6 (S^+_{2B}), corresponding to:

- D0 × KW_A → S^+_{1A} [18.7h, E1] + S^-_{1A} [33.6h, W1]
- D0 × KW_B → S^+_{1B} [17.1h, E1] + S^-_{1B} [40h, W1]
- DE1 × KW_A → S^+_{2A} [18.7h, E2] + S^-_{2A} [33.6h, S0]
- DE1 × KW_B → S^+_{2B} [17.1h, E2] + S^-_{2B} [40.0h, S0]

The results contained in Figure 10 suggest that the prominent WN1 amplitudes found in NGIMS CO_2 thermospheric abundances during November-December 2015 (ref. Figures 5-8) are the signature of D0. The large DE1 signature in MCS temperature near 80 km is largely absent in the thermospheric densities. The not exact correspondence between the MCS and NGIMS pseudo-longitude spectra is not surprising and may be explained by several factors, including (a) differences in the MCS and NGIMS latitude sampling, (b) different dissipation characteristics for the wave components as they propagate from ∼80 km to ∼150 km and above, (c) additional nonlinear interactions occurring between ∼80 km to ∼150 km that may reduce the wave amplitudes, (d) differences between the temperature and density fields, (e) contributions from semidiurnal tides and SPWs in the NGIMS spectra. Nevertheless, the presence of both primary and secondary waves in Figure 10 provides strong evidence that the UFKW-tidal interactions are likely occurring at or below 80 km altitude. Follow-on work may explore the propagation of primary and secondary waves from the lower atmosphere. This analysis would be geared toward understanding at what height and in what latitude regions the interactions may be occurring. This investigation would shed new light onto processes related to nonlinear wave-wave interactions with direct implications for the altitude-longitude variability of the aerobraking densities.

6 Summary and Conclusions

A key element for successful aerobraking operations is developing a capability for improved atmospheric density predictions in the whole Martian thermosphere (∼100-200 km altitude). Prior observational and modeling studies demonstrated that much of the global-scale longitudinal and day-to-day variability of Mars' thermosphere is connected with solar tides, ultra-fast Kelvin waves (UFKWs), and secondary waves associated with their nonlinear interactions. Despite recent progress enabled by combined measurements from the MAVEN and MRO missions, understanding the variability and impacts of the upward-propagating global-scale wave spectrum remains challenging. In this work, over 5 years (∼2015-2020) of MAVEN/NIGIMS CO_2 density near ∼150-200 km and 2 years (∼2015-2016) of MRO/MCS temperatures near 80 km are employed to reveal prominent impacts on Mars' thermospheric density from global-scale waves of lower atmospheric origin, including tides, UFKWs, and secondary waves due to their nonlinear interactions.

Our results and conclusions are summarized as follows:

1. UFKW packets with zonal wavenumber s = -1 and periods between 2.5 and 4.5 days are a common, prominent (∼10-20% amplitude), and persistent feature of Mars' thermosphere (∼150-200 km) and generate significant longitudinal variability at all heights. While their amplitudes are largest at low latitudes (±30°), in accordance with their equatorially-trapped nature, non-negligible (∼5-10%) thermospheric amplitudes can occur even at higher latitudes.

2. Nonlinear interactions between UFKW packets and solar tides produce secondary waves with thermospheric amplitudes that may exceed those of the primary waves that produced them.
3. Detailed analyses focused on a period of enhanced 2.5-day UFKW1 amplitudes in late 2015, when NGIMS samples low latitudes and MCS data display consistent UFKW signatures, demonstrate:
   (a) primary and secondary wave amplitudes growing twofold with altitude from ∼5-15% near 150 km to ∼12-25% near 200 km,
   (b) combined effects from primary and secondary waves to account for up to ∼80% of the altitude-longitudinal variability of Mars thermospheric density.
4. Concurrent temperature observations near 80 km confirm vertical propagation of the primary and secondary waves from the middle atmosphere and show significant latitudinal asymmetries in the UFKW amplitudes that we surmise may be associated with the effect of mean winds.

This study demonstrates that, similarly to Earth, UFKW packets with periods between about 2.5 and 4.5 days and their interactions with tides are responsible for significant longitudinal variability in the whole Martian thermosphere that should be accounted for when analyzing satellite observations and nonlinear models.

7 Data Availability Statement

The MAVEN/NGIMS level 2 data (version 8 revision 1) and the MRO/MCS temperature data (version v4) used in this work are archived in NASA's Planetary Data System (PDS) at `https://pds-atmospheres.nmsu.edu/data_and_services/atmospheres_data/MAVEN/ngims.html` (Benna & Lyness, 2014) and `https://atmos.nmsu.edu/data_and_services/atmospheres_data/MARS/atmosphere_temp_prof.html` (McCleese et al., 2007), respectively.

Acknowledgments

FG acknowledges support from the NASA Mars Data Analysis (MDAP) grant 80NSSC21K1821 to Orion Space Solutions.

References

References

Angelats i Coll, M., F. Forget, M. A. Lopez-Valverde, P. L. Read, and S. R. Lewis (2004), Upper atmosphere of Mars up to 120 km: Mars Global Surveyor accelerometer data analysis with the LMD general circulation model, J. Geophys. Res., 109, E01011, doi:10.1029/ 2003JE002163.

Banfield, D., B. J. Conrath, P. J. Gierasch, R. J. Wilson, and M. D. Smith (2004), Travelling waves in the Martian atmosphere from MGS TES Nadir data, Icarus, 170, 365–403, doi:10.1016/j.icarus.2004.03.015.

Benna M., E. Lyness (2014), MAVEN Neutral Gas and Ion Mass Spectrometer Data, NASA Planetary Data System, doi:10.17189/1518931

Bougher, S. W. (1995), Comparative thermospheres: Venus and Mars, Adv. in Sp. Res., 15(4), 21-45, doi:10.1016/0273- 1177(94)00062-6

Bougher, S. W., Engel, S., Roble, R. G., and Foster, B. (1999), Comparative terrestrial planet thermospheres: 2. Solar cycle variation of global structure and winds at equinox, J. Geophys. Res., 104(E7), 16,591-16,611, doi:10.1029/1998JE001019

Bougher, S. W., Engel, S., Roble, R. G., and Foster, B. (2000), Comparative terrestrial planet thermospheres: 3. Solar cycle variation of global structure and winds at solstices, J. Geophys. Res., 105(E7), 17669-17692, doi:10.1029/1999JE001232

Bougher, S. W., T. M. McDunn, K. A. Zoldak, and J. M. Forbes (2009), Solar cycle variability of Mars dayside exospheric temperatures: Model evaluation of underlying thermal balances, Geophys. Res. Lett., 36, L05201, doi:10.1029/2008GL036376.

Bougher, S., D. Pawlowski, J. Bell, S. Nelli, T. McDunn, J. Murphy, M. Chizek, and A. Ridley (2015), Mars Global Ionosphere-Thermosphere Model: Solar cycle, seasonal, and diurnal variations of the Mars upper atmosphere, J. Geophys. Res. Planets, 120, 311-342, doi:10.1002/2014JE004715.

Bougher, S. W., Roeten, K. J., Olsen, K., Mahaffy, P. R., Benna, M., Elrod, M., ... and Jakosky, B. M. (2017). The structure and variability of Mars dayside thermosphere from MAVEN NGIMS and IUVS measurements: Seasonal and solar activity trends in scale heights and temperatures. Journal of Geophysical Research: Space Physics, 122(1), 1296-1313.

Coy, L., & Hitchman, M. (1984). Kelvin wave packets and flow acceleration: A comparison of modeling and observations. Journal of the Atmospheric Sciences, 41, 1875–1880. https://doi.org/10.1175/1520-0469(1984)041¡1875:KWPAFA¿2.0.CO;2

Creasey, J. E., Forbes, J. M. & Hinson, D. P. (2006). Global and seasonal distribution of gravity wave activity in Mars' lower atmosphere derived from MGS radio occultation data. Geophys. Res. Lett. 33, L01803 .

England, S. L., Liu, G., Withers, P., Yiğit, E., Lo, D., Jain, S., Schneider, N. M., Deighan, J., McClintock, W. E., Mahaffy, P. R., Elrod, M., Benna, M., & Jakosky, B. M. (2016). Simultaneous observations of atmospheric tides from combined in situ and remote observations at Mars from the MAVEN spacecraft. Journal of Geophysical Research: Planets, 121, 594–607.

England, S. L., Liu, G., Yiğit, E., Mahaffy, P. R., Elrod, M., Benna, M., Nakagawa, H., Terada, N., and Jakosky, B. (2017), MAVEN NGIMS observations of atmospheric gravity waves in the Martian thermosphere, J. Geophys. Res. Space Physics, 122, 2310-2335, doi:10.1002/2016JA023475.

England, S. L., Liu, G., Kumar, A., Mahaffy, P. R., Elrod, M., Benna, M., Jain, S., Deighan, J., Schneider, N. M., McClintock, W. E., & Evans, J. S. (2019). Atmospheric tides at high latitudes in the Martian upper atmosphere observed by MAVEN and MRO. Journal of Geophysical Research: Space Physics, 124, 2943–2953. https://doi.org/10.1029/2019JA026601

Fang, X., Forbes, J. M., Gan, Q., Liu, G., Thaller, S., Bougher, S., et al. (2021). Tidal effects on the longitudinal structures of the Martian thermosphere and topside ionosphere observed by MAVEN. Journal of Geophysical Research: Space Physics, 126, e2020JA028562. https://doi.org/10.1029/2020JA028562

Forbes, J. M., and M. E. Hagan (2000), Diurnal Kelvin wave in the atmosphere of Mars: Towards an understanding of stationary density structures observed by the MGS accelerometer, Geophys. Res. Lett., 27(21), 3563-3566.

Forbes, J.M., Bridger, A.F.C., Bougher, S.W., Hagan, M.E., Hollingsworth, J.L., Keating, G.M., and J. Murphy (2002), Nonmigrating tides in the thermosphere of Mars, J. Geophys. Res., 107(E11), 5113, doi:10.1029/2001JE001582.

Forbes, J. M., Lemoine, F. G., Bruinsma, S. L., Smith, M. D., & Zhang, X. (2008). Solar flux variability of Mars' exosphere densities and temperatures. Geophysical Research Letters, 35(1), L01201. https://doi.org/10.1029/2007gl031904

Forbes, J. M., Zhang, X., Palo, S. E., Russell, J., Mertens, C. J., & Mlynczak, M. (2009). Kelvin waves in stratosphere, mesosphere and lower thermosphere temperatures as observed by TIMED/SABER during 2002–2006. Earth Planets and Space, 61(4), 447–453. https://doi.org/1 0.1186/bf03353161

Forbes, J. M. (2017). Wave coupling and nonlinear interactions in the atmospheres of Earth and Mars. Quart. Physical Review, 3(3), 1-18.

Forbes, J. M., Zhang, X., Maute, A., & Hagan, M. E. (2018). Zonally symmetric oscillations of the thermosphere at planetary wave periods. Journal of Geophysical Research: Space Physics, 123, 4110–4128. https://doi.org/10.1002/2018JA025258

Forbes, J. M., Zhang, X., Forget, F., Millour, E., & Kleinböhl, A. (2020a). Solar tides in the middle and upper atmosphere of Mars. Journal of Geophysical Research: Space Physics, 125, e2020JA028140. https://doi.org/10.1029/2020JA028140

Forbes, J. M., Maute, A., & Zhang, X.(2020b). Dynamics and electrodynamics of an ultra-fast Kelvin wave (UFKW) packet in the ionosphere-thermosphere (IT). Journal of Geophysical Research: Space Physics, 125, e2020JA027856. https://doi.org/10.1029/2020JA027856

Forbes, J. M., Bruinsma, S., Zhang, X., Forget, F., Marty, J.-C., Millour, E., & González-Galindo, F. (2021). The wave origins of longitudinal structures in ExoMars Trace Gas Orbiter (TGO) aerobraking densities. Journal of Geophysical Research: Space Physics, 126, e2020JA028769. https://doi.org/10.1029/2020JA028769

Forbes, J. M., Zhang, X., Fang, X., Benna, M., González-Galindo, F., Forget, F., & Millour, E. (2023a). Solar-synchronous tides in Mars thermosphere CO2, Ar, and N2 densities from MAVEN. Journal of Geophysical Research: Space Physics, 128, e2023JA031637. https://doi. org/10.1029/2023JA031637

Forbes, J. M., Zhang, X., & Palo, S. E. (2023b). UFKW propagation in the dissipative thermosphere. Journal of Geophysical Research: Space Physics, 128, e2022JA030921. https://doi. org/10.1029/2022JA030921

Gasperini, F., Forbes, J. M., Doornbos, E. N., and Bruinsma, S. L. (2015), Wave coupling between the lower and middle thermosphere as viewed from TIMED and GOCE, J. Geophys. Res. Space Physics, 120, 5788-5804, doi:10.1002/2015JA021300.

Gasperini, F., Hagan, M. E., & Zhao, Y. (2017). Evidence of tropospheric 90 day oscillations in the thermosphere. Geophysical Research Letters, 44, 10,125–10,133. https://doi.org/10.1002/2017GL075445

Gasperini, F., Hagan, M. E., and Forbes, J. M. (2018). Seminal evidence of a 2.5-sol ultra-fast Kelvin wave in Mars' middle and upper atmosphere, Geophys. Res. Lett.,45, 6324-6333, doi:10.1029/2018GL077882.

Gasperini, F., Liu, H., and McInerney, J. (2020), Preliminary evidence of Madden-Julian Oscillation effects on ultrafast tropical waves in the thermosphere, J. Geophys. Res.Space Physics, 125, e2019JA027649, doi:10.1029/2019JA027649.

Gasperini, F., Crowley, G., Immel, T. J., and Harding, B. J. (2022). Vertical wave coupling in the low-latitude ionosphere-thermosphere as revealed by concurrent ICON and COSMIC-2 observations. Space Sci. Rev. 218, 55. doi:10.1007/s11214-022-00923-1

Gasperini, F., Hughes, J., & Thiemann, E. M. B. (2023). Solar rotation effects in Earth's and Mars' thermospheric densities as revealed by concurrent MAVEN, Swarm-C, and GOES observations. Journal of Geophysical Research: Planets, 128, e2022JE007431. https://doi.org/10.1029/2022JE007431

Gu, S.-Y., Dou, X., Lei, J., Li, T., Luan, L., Wan, W., & Russell, J. M. III (2014). Ionospheric response to the ultrafast Kelvin wave in the MLT region. Journal of Geophysical Research: Space Physics, 119, 1369–1380. https://doi.org/10.1002/2013JA019086

Guzewich, S. D., E. R. Talaat, and D. W. Waugh (2012), Observations of planetary waves and nonmigrating tides by the Mars Climate Sounder, J. Geophys. Res., 117, E03010, doi:10.1029/2011JE003924.

Guzewich, S. D., R. J. Wilson, T. H. McConnochie, A. D. Toigo, D. J. Banfield, and M. D. Smith (2014), Thermal tides during the 2001 Martian global-scale dust storm, J. Geophys. Res. Planets, 119, doi:10.1002/2013JE004502.

Hayashi, Y. (1971). A generalized method of resolving disturbances into progressive and retrogressive waves by space Fourier and time cross-spectral analyses, J. Meteorol. Soc. Jpn. Ser. II, 49, 125-128, doi:10.2151/jmsj1965.49.2_125.

Hughes, J., Gasperini, F., and Forbes, J. M. (2022). Solar rotation effects in Martian thermospheric density as revealed by five years of MAVEN observations, J. Geophys. Res. Planets, 127, e2021JE007036. https://doi.org/10.1029/2021JE007036

Jakosky, B.M., Lin, R.P., Grebowsky, J.M. et al. (2015). The Mars Atmosphere and Volatile Evolution (MAVEN) Mission. Space Sci Rev 195, 3-48. https://doi.org/10.1007/s11214-015-0139-x

Jenkins G., S. W. Bougher, R. Lugo, R. H. Tolson, R. W. Zurek, D. Baird, L. Steele, D. Kass, P. Withers, MAVEN Accelerometer Observations of Thermospheric Densities During Aerobraking and Deep Dip 2: Wave Features and Connections to Upward Propagating Thermal Tides, Journal of Geophysical Research: Planets, 10.1029/2022JE007535, 128, 4, (2023).

Kumar, A., England, S. L., Liu, G., Jain, S., & Schneider, N. M. (2022). Observations of atmospheric tides in the middle and upper atmosphere of Mars from MAVEN and MRO. Journal of Geophysical Research: Planets, 127, e2022JE007290 https://doi.org/10.1029/2022JE007290

Lee, C., W. G. Lawson, M. I. Richardson, N. G. Heavens, A. Kleinbohl, D. Banfield, D. J. McCleese, R. W. Zurek, D. Kass, J. T. Schofield, C. B. Leovy, F. W. Taylor, and A. D. Toigo., (2009), Thermal tides in the Martian middle atmosphere as seen by the Mars Climate Sounder, J. Geophys. Res., 114, E03005, doi:10.1029/2008JE003285.

Liu, G., England, S. L., Immel, T. J., Frey, H. U., Mannucci, A. J., & Mitchell, N. J. (2015). A comprehensive survey of atmospheric quasi 3 day planetary-scale waves and their impacts on the day-to-day variations of the equatorial ionosphere. Journal of Geophysical Research: Space Physics, 120, 2979–2992. https://doi.org/10.1002/2014JA020805

Liu, G., England, S., Lillis, R. J., Mahaffy, P. R., Elrod, M., Benna, M., & Jakosky, B. (2017). Longitudinal structures in mars-upper atmosphere as observed by MAVEN/NGIMS. Journal of Geophysical Research: Space Physics, 122, 1258–1268. https://doi.org/10.1002/2016JA023455

Liu, G., England, S. L., Lillis, R. J., Withers, P., Mahaffy, P. R., Rowland, D. E., et al. (2018). Thermospheric expansion associated with dust increase in the lower atmosphere on Mars observed by MAVEN/NGIMS. Geophysical Research Letters, 45, 2901–2910. https://doi.org/10.1002/2018GL077525

Liu, J., Jin, S., & Li, Y. (2019). Seasonal variations and global wave distributions in the Mars thermosphere from MAVEN and multisatellites accelerometer-derived mass densities. Journal Geophysical Research: Space Physics, 124, 9315–9334. https://doi.org/10.1029/2019JA026720

Lo, D. Y., Yelle, R. V., Schneider, N. M., Jain, S. K., Stewart, A. I. F., England, S. L., Deighan, J. I., Stiepen, A., Evans, J. S., Stevens, M. H., et al. (2015), Nonmigrating tides in the Martian atmosphere as observed by MAVEN IUVS, Geophys. Res. Lett., 42, 9057–9063, doi:10.1002/2015GL066268.

Lott, F., Denvil, S., Butchart, N., Cagnazzo, C., Giorgetta, M. A., Hardiman, S. C., Manzini, E., Krismer, T., Duvel, J.-P., Maury, P., Scinocca, J. F., Watanabe, S., & Yukimoto, S. (2014). Kelvin and Rossby-gravity wave packets in the lower stratosphere of some high-top CMIP5 models. Journal of Geophysical Research: Atmospheres, 119, 2156-2173. https://doi.org/10.1002/2013JD020797

Mahaffy, P. R., et al. (2014), The neutral gas and ion mass spectrometer on the Mars Atmosphere and Volatile Evolution Mission, Space Sci. Rev., 185, doi:10.1007/s11214-11014-10091-11211.

Mahaffy, P. R., M. Benna, M. Elrod, R. V. Yelle, S. W. Bougher, S. W. Stone, and B. M. Jakosky (2015), Structure and composition of the neutral upper atmosphere of Mars from the MAVEN NGIMS investigation, Geophys. Res. Lett., 42, 8951-8957, doi:10.1002/2015GL065329.

McCleese, D. J., Schofield, J. T., Taylor, F. W., Calcutt, S. B., Foote, M. C., Kass, D. M., Leovy, C. B., Paige, D. A., Read, P. L., and Zurek, R. W. (2007), Mars Climate Sounder: An investigation of thermal and water vapor structure, dust and condensate distributions in the atmosphere, and energy balance of the polar regions, J. Geophys. Res., 112, E05S06, doi:10.1029/2006JE002790.

Moudden, Y., and J. M. Forbes (2010), A new interpretation of Mars aerobraking variability: Planetary wave-tide interactions, J. Geophys. Res., 115, E09005, doi:10.1029/2009JE003542.

Moudden, Y., and J. M. Forbes (2011a), First detection of wave interactions in the middle atmosphere of Mars, Geophys. Res . Lett., 38, L04202, doi:10.1029/2010GL045592.

Moudden, Y., and J. M. Forbes (2011b), Simulated planetary wave-tide interactions in the atmosphere of Mars, J. Geophys. Res., 116, E01004, doi:10.1029/2010JE003698.

Moudden, Y., and J. M. Forbes (2015), Density prediction in Mars' aerobraking region, Space Weather, 13, 86-96, doi:10.1002/2014SW001121.

Mridula, N., and Manju, G. (2021). On the seasonal evolution of the diurnal pattern of the longitudinal structures in MAVEN NGIMS derived CO2 densities over Martian upper atmosphere. Journal of Atmospheric and Solar-Terrestrial Physics, 212, 105508.

Nystrom, V., Gasperini, F., Forbes, J. M., & Hagan, M. E. (2018). Exploring wave-wave interactions in a general circulation model. Journal of Geophysical Research: Space Physics, 123, 827–847. https://doi.org/10.1002/2017JA024984

Teitelbaum, H., and F. Vial (1991), On tidal variability induced by nonlinear interaction with planetary waves, J. Geophys. Res, doi: 10.1029/91JA01019.

Terada, N., et al. (2017), Global distribution and parameter dependences of gravity wave activity in the Martian upper thermosphere derived from MAVEN/NGIMS observations, J. Geophys. Res. Space Physics, 122, 2374–2397, doi:10.1002/2016JA023476.

Thaller, S. A., Andersson, L., Pilinski, M. D., Thiemann, E., Withers, P., Elrod, M., et al. (2020). Tidal wave-driven variability in the Mars ionosphere-thermosphere system. Atmosphere, 11(5), 521. https://doi.org/10.3390/atmos11050521

Thaller, S. A., Andersson, L., E. Thiemann, M. D. Pilinski, et al. (2023), Martian nonmigrating atmospheric tides in the thermosphere and ionosphere at solar minimum, Icarus, 10.1016/j.icarus.2021.114767, 393, (114767).

Tolson, R.H., Keating, G.M., Cancro, G.J., Parker, J.S., Noll, S.N., and Wilkerson, B.L. (1999), Application of Accelerometer Data to Mars Global Surveyor Aerobraking Operations, J. Spacecr. Rockets, 36(3), 323-329.

Tolson, R.H., Dwyer, A.M., Hanna, J.L., Keating, G.M., George, B.E., Escalera, P.E., and Werner, M.R. (2005), Applications of Accelerometer Data to Mars Odyssey Aerobraking and Atmospheric Modeling, J. Spacecr. Rockets, 42(3), 435-443.

Tolson, R., E. Bemis, S. Hough, K. Zaleski, G. Keating, J. Shidner, S. Brown, A. Brickler, M. Scher, and P. Thomas (2008), Atmospheric modeling using accelerometer data during Mars Reconnaissance Orbiter aerobraking operations, J. Spacecr. Rockets, 45, 511-518, doi:10.2514/1.34301.

VanderPlas, J. T. (2018). Understanding the Lomb–Scargle periodogram. The Astrophysical Journal Supplement Series, 236(1), 16. https://doi.org/10.3847/1538-4365/aab766

Wilson, R. J. (2002), Evidence for nonmigrating thermal tides in the Mars upper atmosphere from the Mars Global Surveyor Accelerometer Experiment, Geophys. Res. Lett., 29(7), 1120-1123, doi:10.1029/2001GL013975.

Wu, Z., Li, T., & Dou, X. (2015). Seasonal variation of martian middle atmosphere tides observed by the mars climate sounder. Journal of Geophysical Research: Planets, 120, 2206–2223. https://doi.org/10.1002/2015JE004922

Yamazaki, Y. (2023). A method to derive Fourier-wavelet spectra for the characterization of global-scale waves in the mesosphere and lower thermosphere and its MATLAB and Python software (fourierwavelet v1. 1). Geoscientific Model Development, 16(16), 4749-4766.

Yiğit, E., Aylward, A. D., & Medvedev, A. S. (2008). Parameterization of the effects of vertically propagating gravity waves for thermosphere general circulation models: Sensitivity study. Journal of Geophysical Research, 113(D19), D19106. https://doi.org/10.1029/2008JD010135

Yiğit, E., S. L. England, G. Liu, A. S. Medvedev, P. R. Mahaffy, T. Kuroda, and B. M. Jakosky (2015), High-altitude gravity waves in the Martian thermosphere observed by MAVEN/NGIMS and modeled by a gravity wave scheme, Geophys. Res. Lett., 42, 8993– 9000, doi:10.1002/2015GL065307.

Yiğit, E., Medvedev, A., Benna, M., & Jakosky, B. (2021). Dust storm-enhanced gravity wave activity in the Martian thermosphere observed by MAVEN and implications for atmospheric escape. Geophysical Research Letters, 48(5), e2020GL092095. https://doi.org/10.1029/2020GL092095

Yiğit, E. (2023). Coupling and interactions across the Martian whole atmosphere system. Nature Geoscience, 16(2), 123–132. https://doi.org/10.1038/s41561-022-01118-7

Zurek, R. W., R. A. Tolson, S. W. Bougher, R. A. Lugo, D. T. Baird, J. M. Bell, and B. M. Jakosky (2017), Mars thermosphere as seen in MAVEN accelerometer data, J. Geophys. Res. Space Physics, 122, 3798-3814, doi:10.1002/2016JA023641.

Figure1.

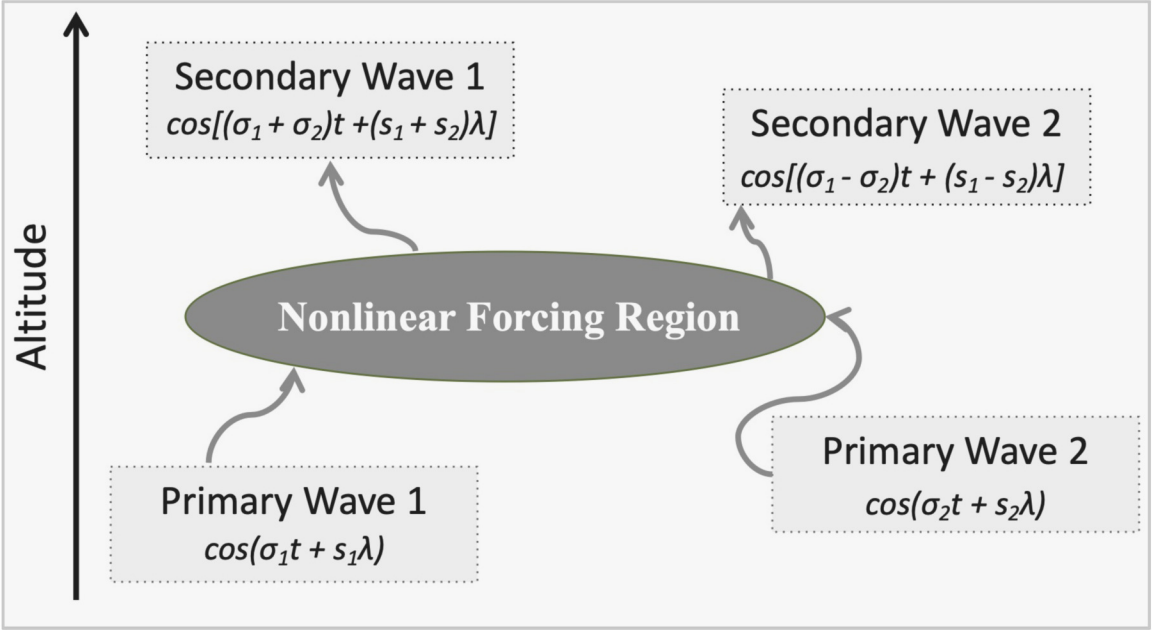
Altitude
Secondary Wave 1
$cos[(\sigma_1 + \sigma_2)t + (s_1 + s_2)\lambda]$
Secondary Wave 2
$cos[(\sigma_1 - \sigma_2)t + (s_1 - s_2)\lambda]$
Nonlinear Forcing Region
Primary Wave 1
$cos(\sigma_1 t + s_1\lambda)$
Primary Wave 2
$cos(\sigma_2 t + s_2\lambda)$

Figure2.

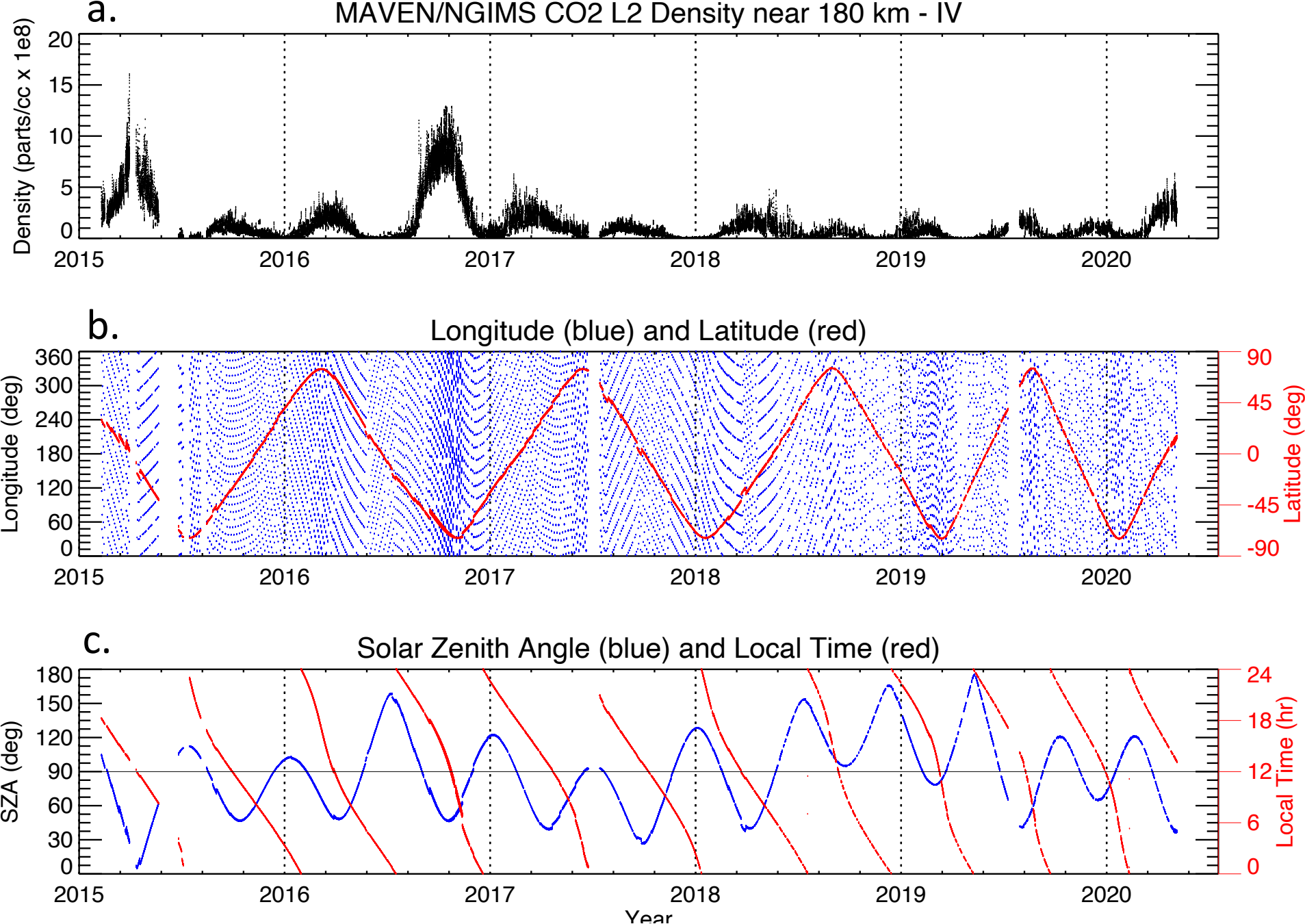
a.
MAVEN/NGIMS CO2 L2 Density near 180 km - IV
Density (parts/cc x 1e8)
20
15
10
5
0
2015
2016
2017
2018
2019
2020
b.
Longitude (blue) and Latitude (red)
Longitude (deg)
360
300
240
180
120
60
0
90
45
0
-45
-90
Latitude (deg)
c.
Solar Zenith Angle (blue) and Local Time (red)
SZA (deg)
180
150
120
90
60
30
0
24
18
12
6
0
Local Time (hr)
Year

Figure3.

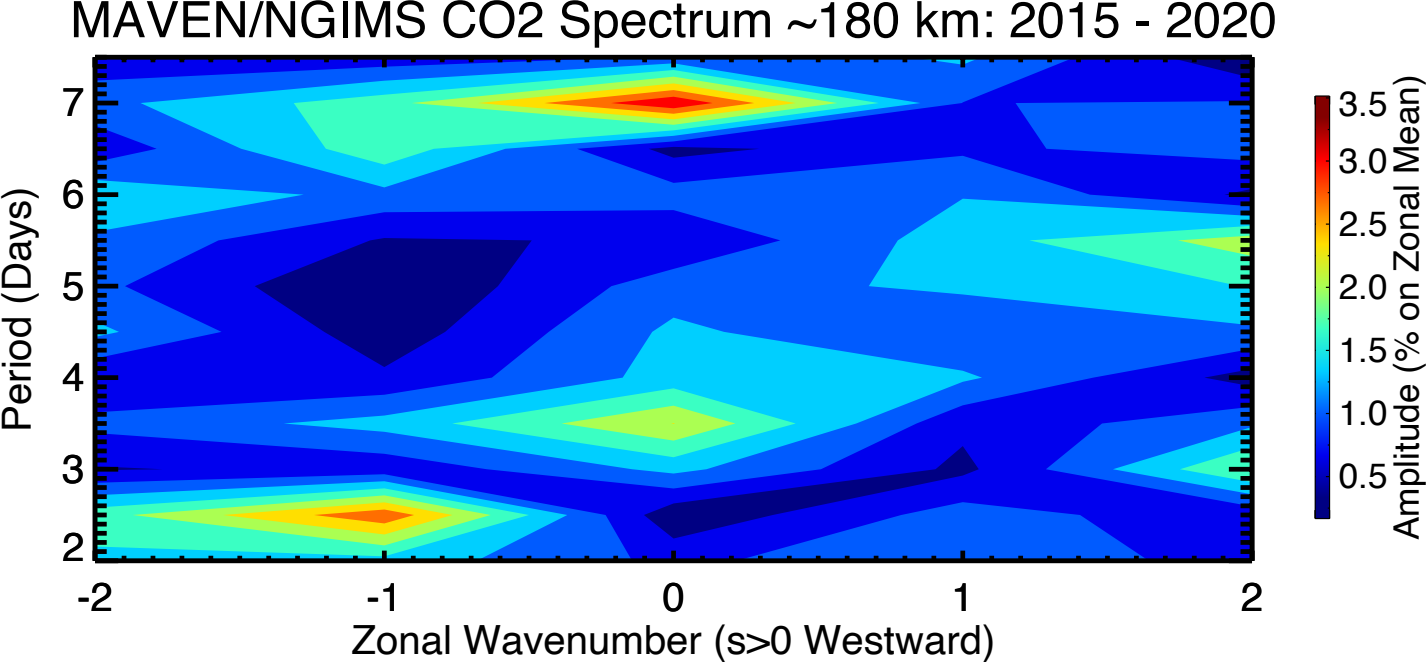
MAVEN/NGIMS CO2 Spectrum ~180 km: 2015 - 2020
Period (Days)
7
6
5
4
3
2
-2
-1
0
1
2
Zonal Wavenumber (s>0 Westward)
3.5
3.0
2.5
2.0
1.5
1.0
0.5
Amplitude (% on Zonal Mean)

Figure4.

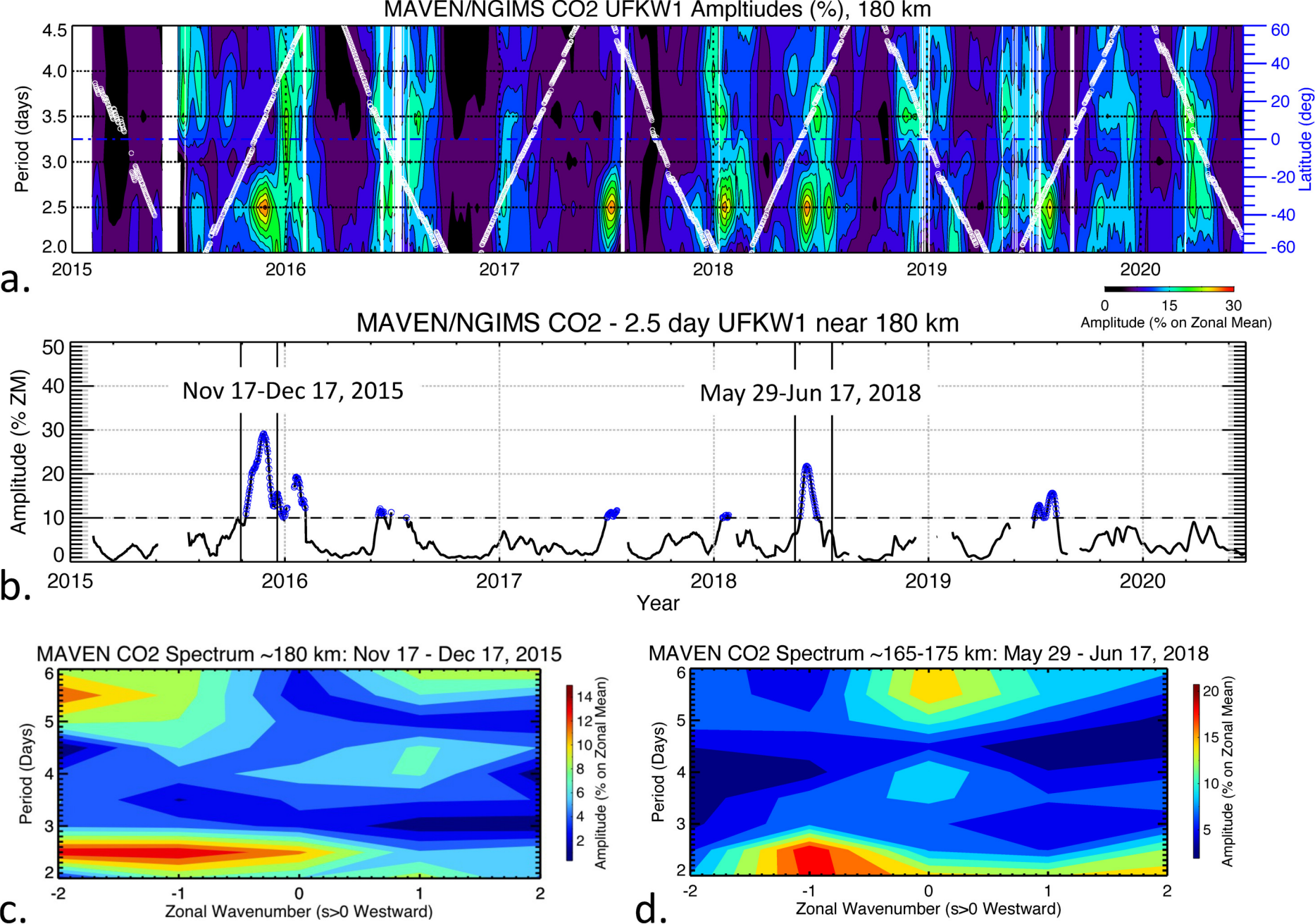
MAVEN/NGIMS CO2 UFKW1 Ampltiudes (%), 180 km
Period (days)
Latitude (deg)
a.
Amplitude (% on Zonal Mean)
MAVEN/NGIMS CO2 - 2.5 day UFKW1 near 180 km
Amplitude (% ZM)
Nov 17-Dec 17, 2015
May 29-Jun 17, 2018
Year
b.
MAVEN CO2 Spectrum ~180 km: Nov 17 - Dec 17, 2015
Period (Days)
Zonal Wavenumber (s>0 Westward)
Amplitude (% on Zonal Mean)
c.
MAVEN CO2 Spectrum ~165-175 km: May 29 - Jun 17, 2018
Period (Days)
Zonal Wavenumber (s>0 Westward)
Amplitude (% on Zonal Mean)
d.

Figure5.

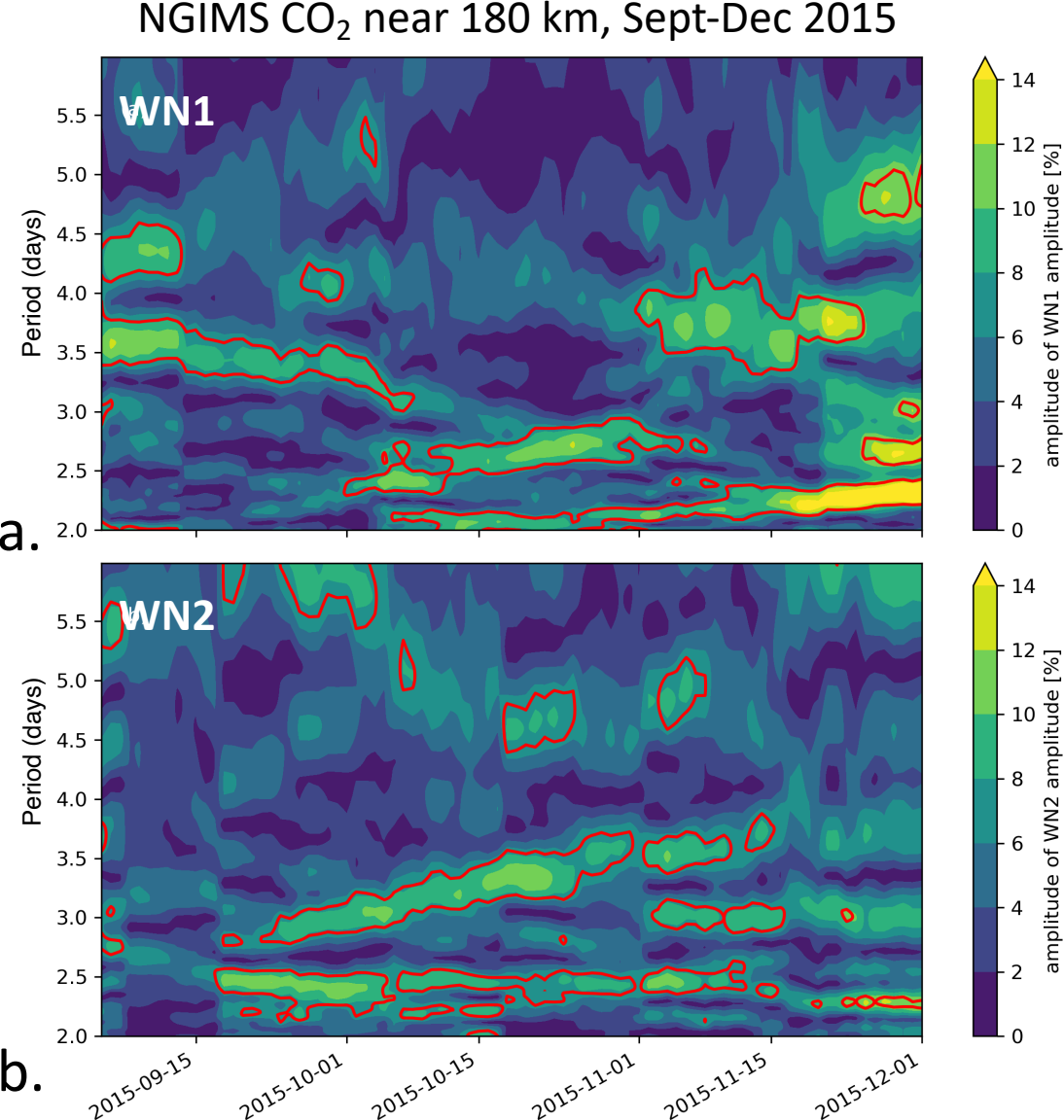
NGIMS CO_2 near 180 km, Sept-Dec 2015
WN1
WN2
Period (days)
5.5
5.0
4.5
4.0
3.5
3.0
2.5
2.0
amplitude of WN1 amplitude [%]
amplitude of WN2 amplitude [%]
14
12
10
8
6
4
2
0
a.
b.
2015-09-15
2015-10-01
2015-10-15
2015-11-01
2015-11-15
2015-12-01

Figure6.

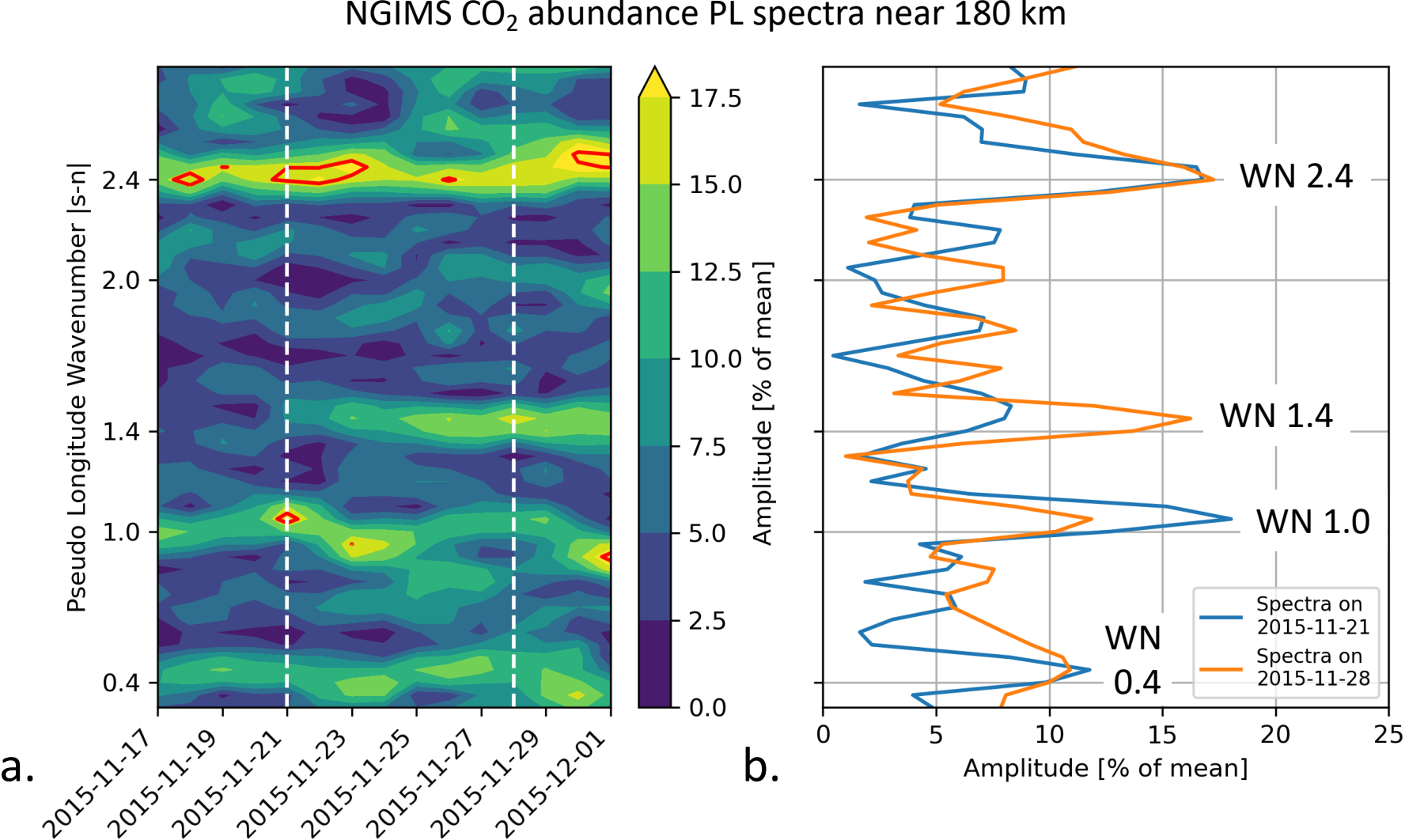
NGIMS CO_2 abundance PL spectra near 180 km
Pseudo Longitude Wavenumber |s-n|
2.4
2.0
1.4
1.0
0.4
2015-11-17
2015-11-19
2015-11-21
2015-11-23
2015-11-25
2015-11-27
2015-11-29
2015-12-01
17.5
15.0
12.5
10.0
7.5
5.0
2.5
0.0
Amplitude [% of mean]
a.
b.
WN 2.4
WN 1.4
WN 1.0
WN 0.4
Spectra on 2015-11-21
Spectra on 2015-11-28
0
5
10
15
20
25
Amplitude [% of mean]

Figure7.

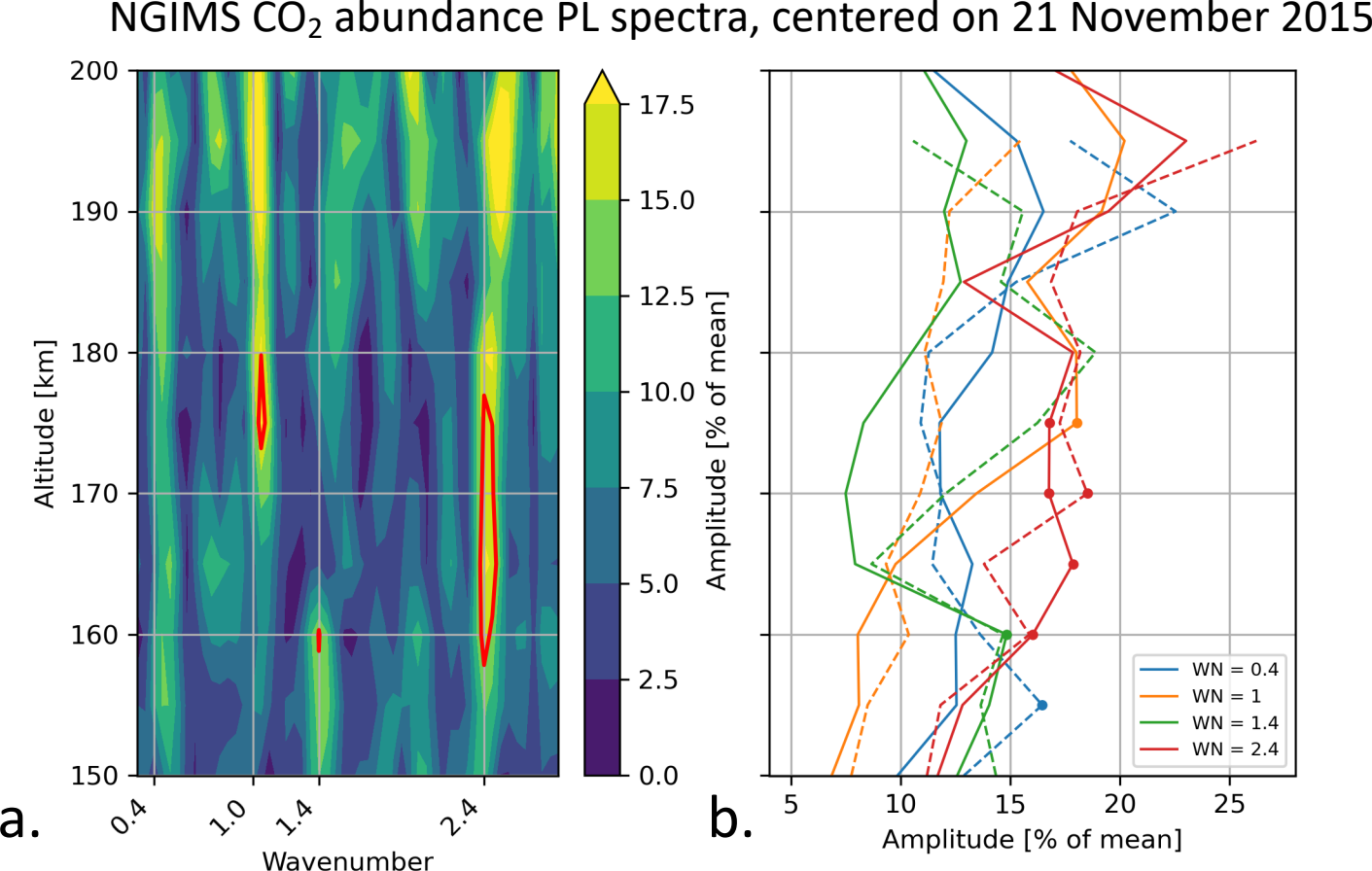
NGIMS CO_2 abundance PL spectra, centered on 21 November 2015
Altitude [km]
200
190
180
170
160
150
17.5
15.0
12.5
10.0
7.5
5.0
2.5
0.0
a.
0.4
1.0
1.4
2.4
Wavenumber
b.
Amplitude [% of mean]
5
10
15
20
25
Amplitude [% of mean]
WN = 0.4
WN = 1
WN = 1.4
WN = 2.4

Figure8.

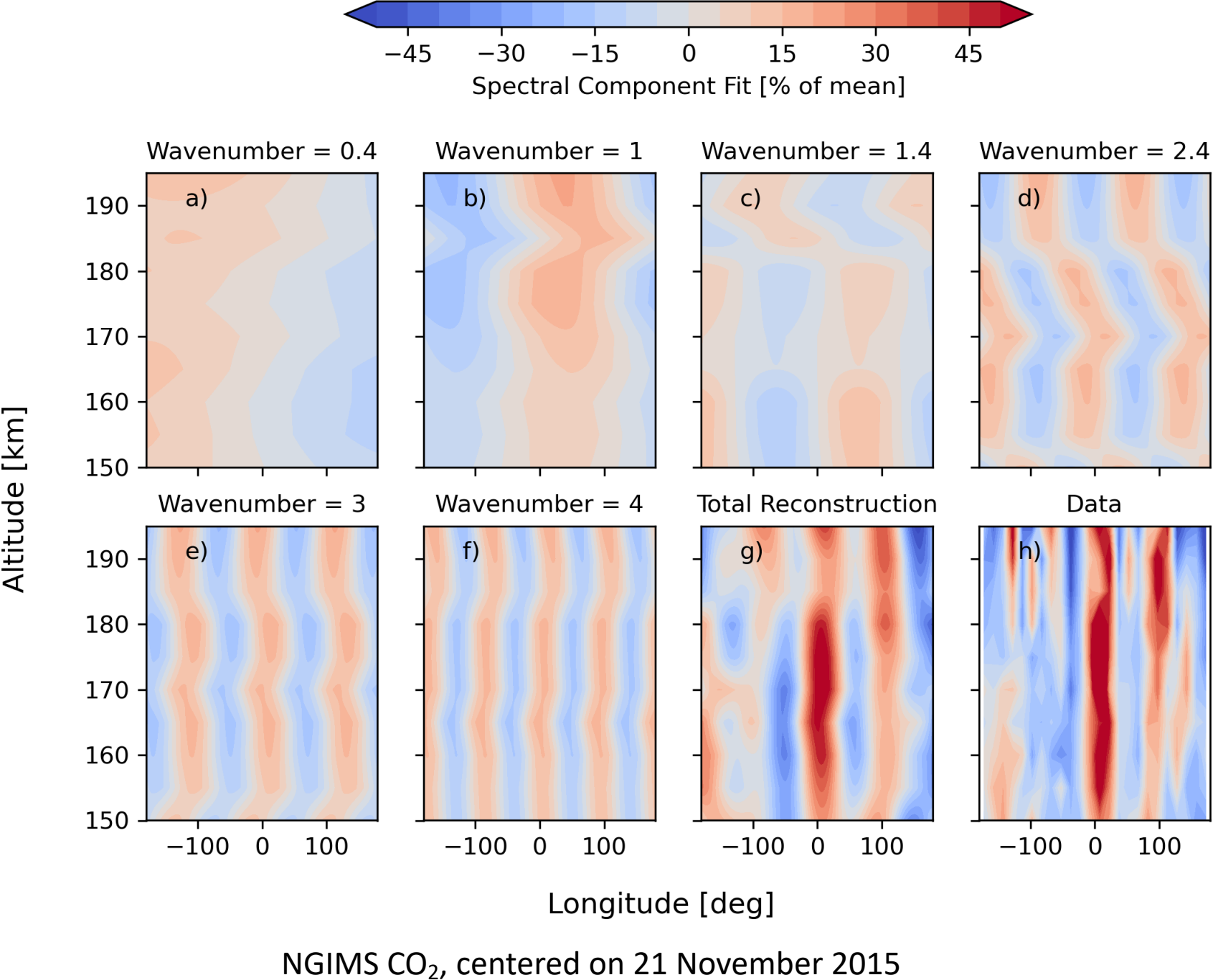
−45
−30
−15
0
15
30
45
Spectral Component Fit [% of mean]
Wavenumber = 0.4
Wavenumber = 1
Wavenumber = 1.4
Wavenumber = 2.4
a)
b)
c)
d)
Wavenumber = 3
Wavenumber = 4
Total Reconstruction
Data
e)
f)
g)
h)
Altitude [km]
190
180
170
160
150
−100
0
100
Longitude [deg]
NGIMS CO_2, centered on 21 November 2015

Figure9.

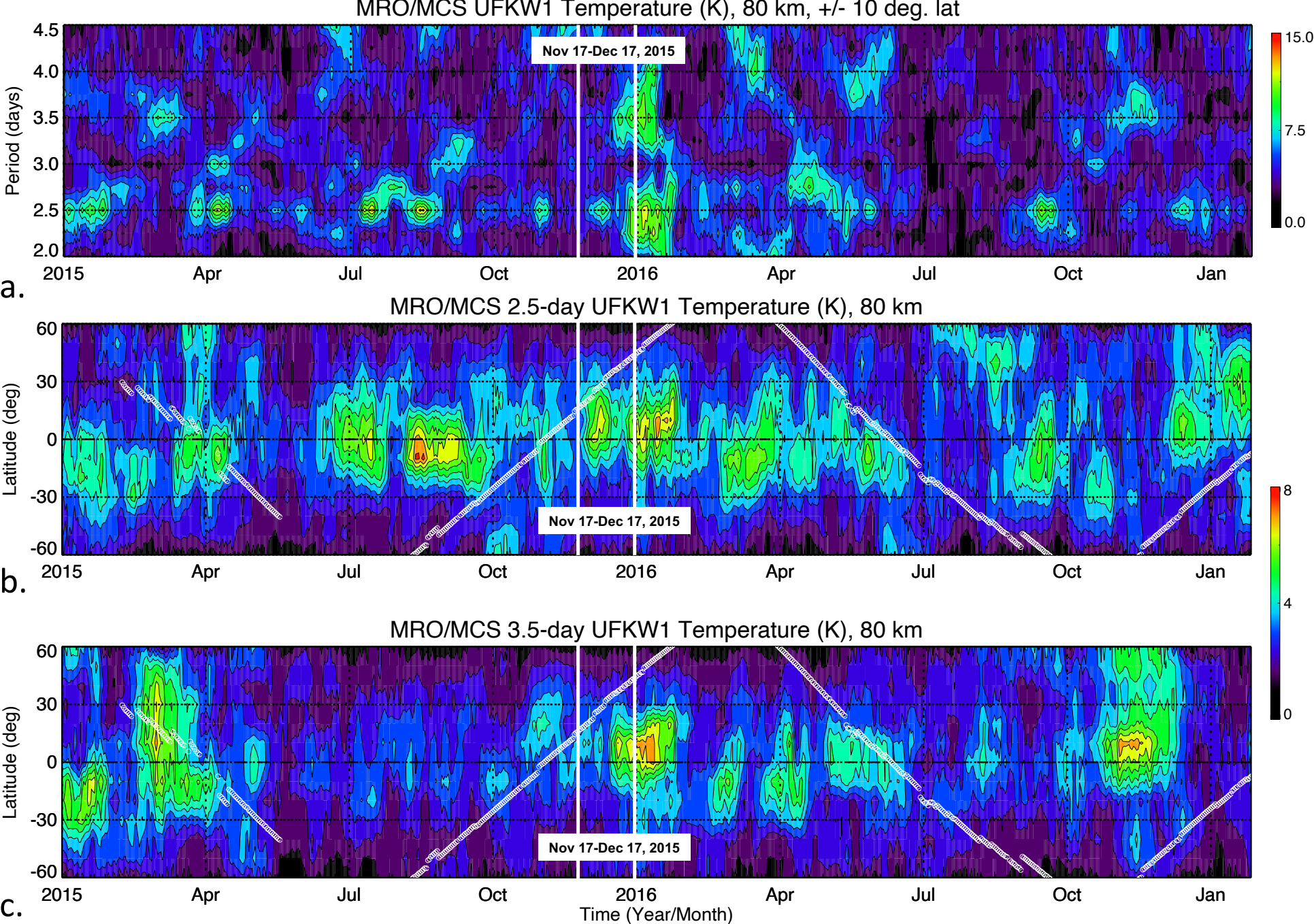
MRO/MCS UFKW1 Temperature (K), 80 km, +/- 10 deg. lat
Period (days)
4.5
4.0
3.5
3.0
2.5
2.0
Nov 17-Dec 17, 2015
15.0
7.5
0.0
2015
Apr
Jul
Oct
2016
Apr
Jul
Oct
Jan
a.
MRO/MCS 2.5-day UFKW1 Temperature (K), 80 km
Latitude (deg)
60
30
0
-30
-60
Nov 17-Dec 17, 2015
8
4
0
b.
MRO/MCS 3.5-day UFKW1 Temperature (K), 80 km
Latitude (deg)
Nov 17-Dec 17, 2015
c.
Time (Year/Month)

Figure10.

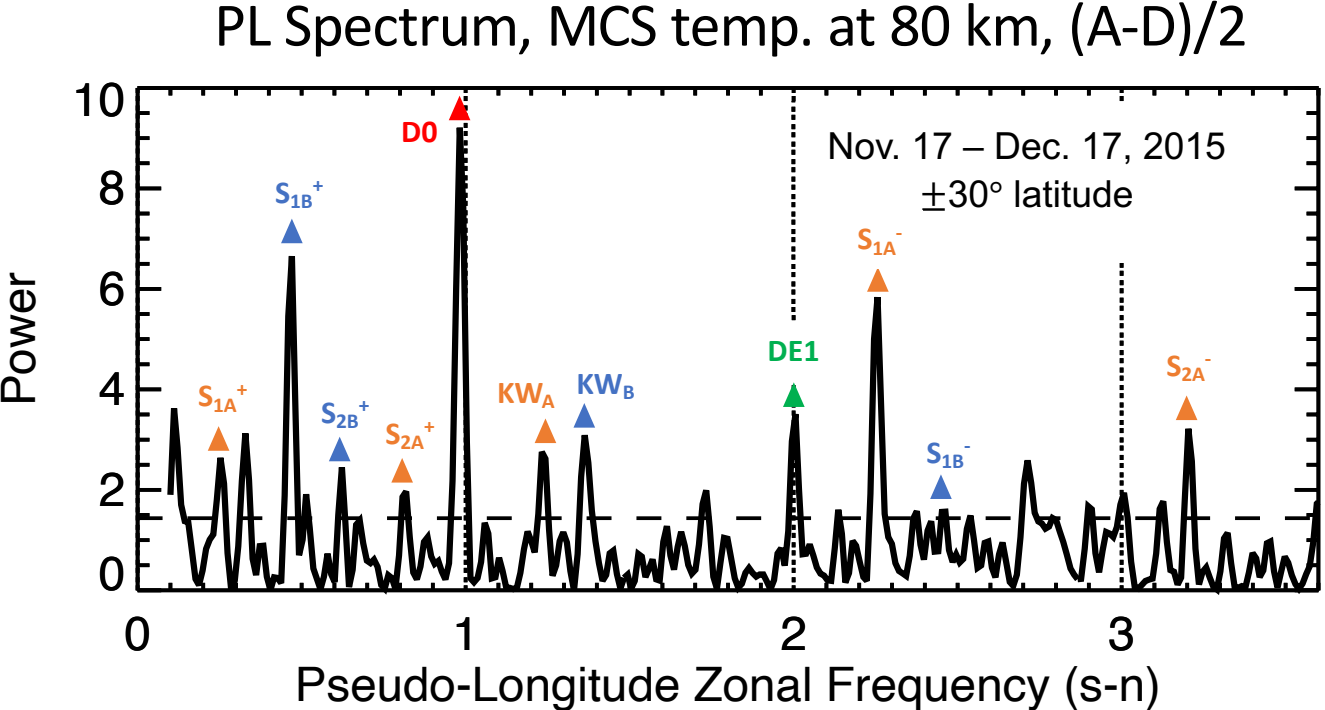

Primary Waves

D0 —> 1.0

DE1 —> 2.0

3.5-day KW_A —> 1.3

2.5-day KW_B —> 1.4

Secondary Waves

D0 x KW_A —> 2.3 (S_{1A}^-), 0.3 (S_{1A}^+)

DE1 x KW_A —> 3.3 (S_{2A}^-), 0.7 (S_{2A}^+)

D0 x KW_B —> 2.4 (S_{1B}^-), 0.4 (S_{1B}^+)

DE1 x KW_B —> 3.4 (S_{2B}^- not obs.), 0.6 (S_{2B}^+)